A magnetically soft yet mechanically strong and ductile Ta free CoFeNi high entropy alloy with Al and Ti additions

nature communications

Article

https://doi.org/10.1038/s41467-026-68891-6

A magnetically soft yet mechanically strong and ductile Ta free CoFeNi high entropy alloy with Al and Ti additions

Received: 14 January 2025

Accepted: 20 January 2026

Published online: 05 February 2026

Check for updates

Sudip Kumar Sarkar[1,7], Nachiket Keskar[2,7], Li Ping Tan[3], Tirthesh Ingale[1,2], Advika Chesetti[2], Sriswaroop Dasari[2,4], Karl P. Davidson[3,5], V. Chaudhary[6] ✉, Narendra Dahotre[1,2], R. V. Ramanujan[3] ✉ & Rajarshi Banerjee[1,2,3] ✉

Next generation high speed, large torque, rotating electrical machines demand materials with an excellent balance of magnetic and mechanical properties. High entropy alloys (HEAs) can exhibit this unique combination of properties, e.g., CoFeNi based HEAs containing Ta. The high Ta content makes these alloys prohibitively expensive for industrial applications. Hence, we develop Ta free HEA using a thermodynamic approach. The addition of Al and Ti to the base CoFeNi alloy is studied. We investigate two compositions: $Ti_{0.24}CoFeNi_{0.78}$ and $Al_{0.3}Ti_{0.2}CoFeNi$. In their solution treated and quenched condition these HEAs exhibit a low coercivity H_c ~ 1.8–2.4 Oe, high saturation magnetization M_s ~ 96.5-137.3 emu/g, coupled with a high yield strength, YS ~ 780-850 MPa, ultimate tensile strength, UTS ~ 1200 MPa, large tensile elongation, ε ~ 29-35%, and with desired high electrical resistivity (~ 269.5-308.3 μΩ·cm), making them attractive for high frequency electrical machines. Importantly, the latter HEA is further strengthened to a very high YS ~ 1140-1200 MPa with excellent ductility (ε ~ 18-25%) and electrical resistivity (296.1-459.3 μΩ·cm), but at the cost of higher H_c values ~ 8.8-48.6 Oe.

Soft magnetic materials (SMMs) play a pivotal role in rotating electrical machines, which underpin a wide range of modern energy conversion and mobility technologies. The rising global emphasis on reducing fossil fuel consumption and greenhouse gas emissions has accelerated the adoption of electric machines in electric vehicles, aircraft, and other technological sectors. According to the U.S. Energy Information Administration's *Monthly Energy Review* (April 2024)[1], nearly 20% of the electrical energy generated in the U.S. power sector is lost before reaching its end use, underscoring the urgent need for improved efficiency in electrical systems. Enhancing efficiency requires materials that combine optimal magnetic, electrical, and mechanical properties, or materials with tunable multifunctional characteristics, to meet the demands of next-generation motors, e.g., for electric vehicles, designed for large torque, high-frequency operation, and more compact architectures[2,3].

The essential requirements for SMMs include: (i) low coercivity (H_c) to minimize hysteresis losses during rapid magnetization–demagnetization cycles, (ii) high saturation magnetization (M_s) for maximizing magnetic flux density and torque, and (iii) elevated electrical resistivity (ρ) to reduce eddy current losses[4–6].

[1]Center for Agile and Adaptive Additive Manufacturing, University of North Texas, Denton, TX, USA. [2]Department of Materials Science and Engineering, University of North Texas, Denton, TX, USA. [3]School of Materials Science and Engineering, Nanyang Technological University, Singapore, Singapore. [4]Department of Metallurgical, Materials, and Biomedical Engineering, University of Texas at El Paso, El Paso, TX, USA. [5]Photon Forge Additive Manufacturing Facility, John de Laeter Centre (JdLC), Curtin University, Perth, WA, Australia. [6]Industrial and Materials Science, Chalmers University of Technology, Gothenburg, Sweden. [7]These authors contributed equally: Sudip Kumar Sarkar, Nachiket Keskar. ✉e-mail: varunc@chalmers.com; ramanujan@ntu.edu.sg; raj.banerjee@unt.edu

Equally critical are superior mechanical properties, particularly high yield strength to prevent plastic deformation under cyclic stresses and adequate ductility for manufacturing flexibility and damage tolerance[7]. Meeting this complex set of requirements would substantially expand the application envelope of SMMs and reduce energy losses across electrical machines.

Despite decades of progress, simultaneously achieving this balance of properties remains a formidable challenge. Conventional SMMs—including Fe–Si silicon steels (3–6 wt.% Si), Fe–Ni permalloys, Fe–Ni–Mo supermalloys, and Fe–Co alloys such as Hiperco 50 and Hiperco 50HS—are widely used in electrical machines. These alloys exhibit low H_c (0.01–5.0 Oe) and high M_s (64–235 emu/g)[7–9] values, yet they fall short in mechanical strength (maximum ~624–810 MPa in Hiperco 50HS)[10–13] and electrical resistivity (27–90 μΩ·cm)[11,14]. Such limitations are particularly acute in high-torque, high-frequency rotor applications in automotive and aviation use cases, where premature mechanical failure and excessive eddy current losses are prevalent[14,15]. Therefore, future progress in electrical machine design hinges on engineering single-composition soft magnetic materials that possess the appropriate magnetic, electrical, and mechanical property set.

Recent advances in high-entropy alloys (HEAs) and complex concentrated alloys (CCAs) have created new opportunities for designing alloys with enhanced multifunctional properties[16,17]. By combining multiple principal magnetic elements, HEAs offer a platform to simultaneously tailor magnetic, structural, and mechanical characteristics[18–20]. The alloying elements and processing conditions are decisive: they influence phase stability, microstructural evolution, and interfacial characteristics, which in turn, can affect the relevant properties[21,22]. HEAs containing concentrated amounts of ferromagnetic elements, such as Co, Fe, and Ni, can exhibit promising soft magnetic properties. Further, the addition of atoms such as Al and Ti, which exhibit large negative enthalpies of mixing with these ferromagnetic elements, promotes chemical ordering within face-centered cubic (FCC) solid solutions, often through the formation of ordered intermetallic nanoprecipitates such as the $L1_2$ or the B2 phases[16,23,24].

The ternary CoFeNi alloy has emerged as a promising base for soft magnetic HEAs. It exhibits excellent magnetic properties[25], and the interaction energies of the three binary pairs (Fe–Ni, Ni–Co, Co–Fe) are nearly zero, yielding a near-ideal random solid solution[21,26]. Equiatomic CoFeNi forms a single-phase FCC structure[16,27], which confers excellent ductility but insufficient mechanical strength[28]. Various strengthening mechanisms have been applied, including solid solution strengthening[29], grain refinement[30], dislocation strengthening[31], and multiphase strengthening[32–35]. Of these, nanoprecipitation strengthening via coherent $L1_2$-type ordered precipitates is especially effective, as established in Ni-based superalloys (γ + γ′ structure)[36], Co-based alloys (e.g., $Co_{84}Ti_8V_8$)[37–39], and Fe-based systems[40–42].

Building on this principle, Al or Ti additions to CoFeNi can induce coherent $L1_2$ nanoprecipitates within the FCC matrix, yielding significant strengthening without severely compromising ductility[21,22,29]. For instance, Han et al.[43] reported a CoFeNi–Ta/Al HEA containing >42 vol.% ordered $L1_2$ nanoprecipitates, which achieved a high yield strength (~1202 MPa) and good tensile ductility (~15%), but exhibited relatively high coercivity (~10.7 Oe). Similarly, Xu et al.[44] studied $(FeCoNi)_{90}–Ti_xAl_y$ alloys, identifying the $(FeCoNi)_{90}–Ti_5Al_5$ composition as optimal. This alloy contained <1 nm nanoprecipitates with ~9.8% volume fraction, yielding a balanced property set: YS = 463 MPa, ductility = 50.7%, M_s = 121.1 emu/g, and H_c = 6.5 Oe.

Phase stability in Co- and Ni-based HEAs is highly sensitive to Al and Ti content. Prior work on Al-containing CoCrFeNi CCAs revealed compositional transitions from FCC/$L1_2$ to FCC/$L1_2$ + BCC/B2, and finally to BCC/B2 with increasing Al content[24,45]. In FCC-based HEAs, Al often stabilizes metastable/stable $L1_2$ and/or B2 nanoprecipitates[36,46]. The simultaneous addition of Ti has proven effective in stabilizing and increasing the mass fraction of the $L1_2$ phase. For example, a CoCrFeNi base alloy with 4 at.% Al + 2 at.% Ti achieved strength ≥1 GPa and ductility ~17%[47], while a CoFeNi base alloy with 8.5 at.% Al + 5.7 at.% Ti reached even higher ductility (~50%) alongside excellent strength[48].

Prior investigations into an $Al_{0.3}$CoFeNi HEA underscored the pivotal role of Al in inducing ordering tendencies[21,22]. This alloy exhibits a combination of long-range ordered (LRO) phases and a disordered FCC solid solution. At 500 °C, $L1_2$ nanoprecipitates enhanced hardness and tensile yield stress, while further thermo-mechanical processing yielded a hierarchical four-phase microstructure (FCC + $L1_2$ + BCC + B2). Depending on the morphology, this complex microstructure delivered exceptional mechanical performance, with the microstructure with multi-scale hierarchical precipitates achieving yield stresses up to ~1490 MPa, ultimate tensile strengths of ~1663 MPa, and ductility of ~12%. However, these mechanical gains were offset by high coercivity (~160 Oe), presenting an opportunity for further microstructure engineering and alloy development.

These findings highlight the central challenge: while introducing ordered nanoprecipitates significantly enhances strength, it often increases coercivity. Achieving a low-coercivity, high-strength microstructure thus requires careful stabilization of nanoscale $L1_2$ phases while avoiding large mass fractions of the magnetically deleterious B2 phase or coarse lamellar morphologies.

In this study, we build upon the previous work on CoFeNi and $Al_{0.3}$CoFeNi alloys by introducing Ti as an additional alloying element to enhance the stability and volume fraction of ordered $L1_2$ nanoprecipitates within an FCC matrix. Solution thermodynamic modeling guided our alloy design. Our central hypothesis is that increasing the fraction of fully coherent nanoscale $L1_2$ precipitates will simultaneously provide high yield strength and preserve low coercivity. As established in superalloy design, Ti is a potent $L1_2$ stabilizer[36], and we hypothesized that its addition to CoFeNi and $Al_{0.3}$CoFeNi-based alloys would yield HEAs with a unique combination of properties: high strength, high ductility, low coercivity, high saturation magnetization, and elevated electrical resistivity. Such alloys would represent a significant advance toward next-generation SMMs for high-frequency, high-torque electrical machines.

Results

Thermodynamic modeling

Pseudo-binary sections of the $Ti_xAl_{0.3}$CoFeNi and Ti–CoFeNi systems, calculated using Thermo-Calc ® with the TCHEA6 database, are shown in Figs. 1a and 1b, respectively. In both cases, alloy compositions were chosen to maximize Ti incorporation while preserving a stable FCC single-phase field at high temperatures: $Al_{0.3}Ti_{0.2}$CoFeNi ($Al_{8.5}Ti_{5.7}Co_{28.5}Fe_{28.5}Ni_{28.5}$ in atom %) for the quinary system and $Ti_{0.24}$CoFeNi$_{0.78}$ ($Ti_8Co_{33}Fe_{33}Ni_{26}$ in atom %) for the quaternary system. The corresponding phase fraction diagrams (Figs. 1b, d) indicate that both alloys transform from a high-temperature FCC phase into multiphase fields containing ordered intermetallics upon cooling. Specifically, the $Al_{0.3}Ti_{0.2}$CoFeNi alloy is predicted to exhibit FCC + $L1_2$ + B2 stability between 800 and 1150 °C, while the $Ti_{0.24}$CoFeNi$_{0.78}$ alloy is expected to form FCC + $L1_2$ phases in this temperature range.

To experimentally validate these predictions, homogenized and cold-rolled (90%) samples of both alloys were solutionized in the high-temperature FCC field (1200 °C for $Al_{0.3}Ti_{0.2}$CoFeNi, 1000 °C for $Ti_{0.24}$CoFeNi$_{0.78}$) and water-quenched. Subsequent annealing treatments were performed within the predicted multiphase regions: the $Al_{0.3}Ti_{0.2}$CoFeNi alloy was annealed at 800 °C for 4 h after solutionizing or, alternatively, annealed directly at 900 °C for 4 h from the cold-rolled state; the $Ti_{0.24}$CoFeNi$_{0.78}$ alloy was annealed at 1000 °C for 15 min. These conditions were selected to promote the evolution of ordered $L1_2$ and B2 phases from the disordered FCC matrix.

https://doi.org/10.1038/s41467-026-68891-6

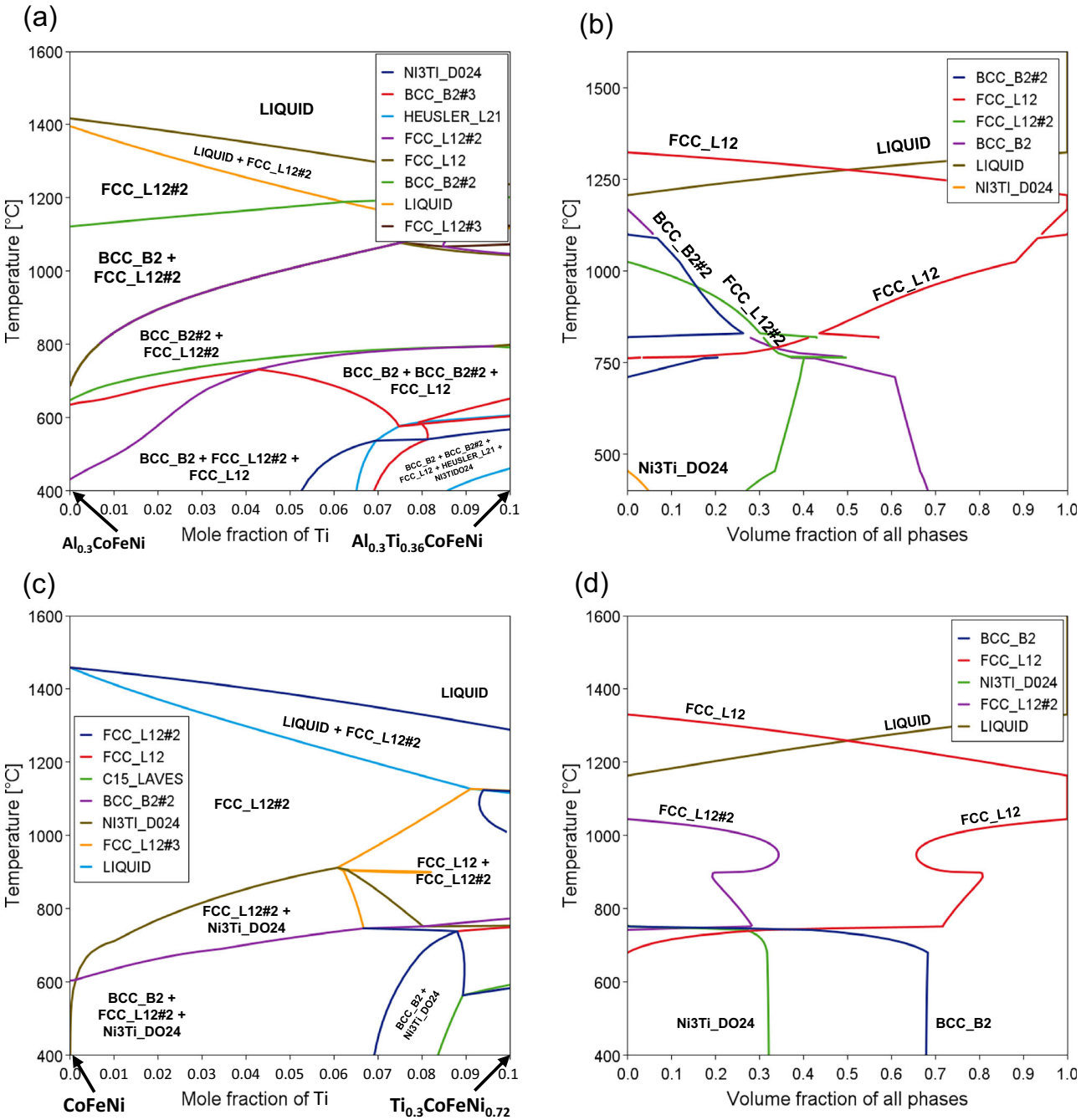

Fig. 1 | Thermodynamic modeling for the Al and Ti-added CoFeNi HEA. **a** Pseudo-binary isopleth showing phase stability in the $Al_{0.3}Ti_{0.2}CoFeNi$ system as a function of temperature and Ti mole fraction varying from $Al_{0.3}CoFeNi$ to $Al_{0.3}Ti_{0.36}CoFeNi$, **b** phase fraction versus temperature for $Al_{0.3}Ti_{0.2}CoFeNi$ showing the expected equilibrium phases in the temperature range of 400–1600 °C, **c** pseudo-binary isopleth showing phase stability in the $Ti_{0.24}CoFeNi_{0.78}$ system as a function of temperature and Ti mole fraction ranging from CoFeNi to $Ti_{0.3}CoFeNi_{0.72}$, and **d** phase fraction versus temperature for the $Ti_{0.24}CoFeNi_{0.78}$ composition showing the expected equilibrium phases in the temperature range of 400–1600 °C.

Evolution of mechanical and magnetic properties

Tensile properties. The tensile behavior of $Ti_{0.24}CoFeNi_{0.78}$ and $Al_{0.3}Ti_{0.2}CoFeNi$ HEAs at room temperature under three different conditions is summarized in Fig. 2a. In the solutionized and water-quenched state (CRSA), the $Ti_{0.24}CoFeNi_{0.78}$ alloy exhibited a yield strength (YS) of ~850 MPa, ultimate tensile strength (UTS) of ~1200 MPa, and elongation to failure of 29%. Under the same condition, the $Al_{0.3}Ti_{0.2}CoFeNi$ alloy showed slightly lower strength (YS ~ 780 MPa, UTS ~ 1110 MPa) but superior ductility (35%). Subsequent isothermal annealing of the solutionized $Al_{0.3}Ti_{0.2}CoFeNi$ alloy at 800 °C for 4 h (CRSA800) markedly enhanced strength, with YS ~ 1200 MPa and UTS ~ 1420 MPa, while maintaining 25% ductility. In the cold-rolled (90%) plus directly annealed (900 °C/4 h) condition (CR900), the alloy displayed YS ~ 1140 MPa, UTS ~ 1500 MPa, and 18% elongation.

For context, the tensile curve of a solutionized CoFeNi alloy is also plotted in Fig. 2a. The comparison highlights the substantial strengthening imparted by Al and Ti additions. Relative to solutionized CoFeNi, the $Al_{0.3}Ti_{0.2}CoFeNi$ HEA in the CRSA state exhibits nearly a threefold increase in YS and a twofold increase in UTS. Remarkably, this strengthening was achieved without significant loss of ductility, pointing to a modified deformation mechanism that mitigates the

https://doi.org/10.1038/s41467-026-68891-6

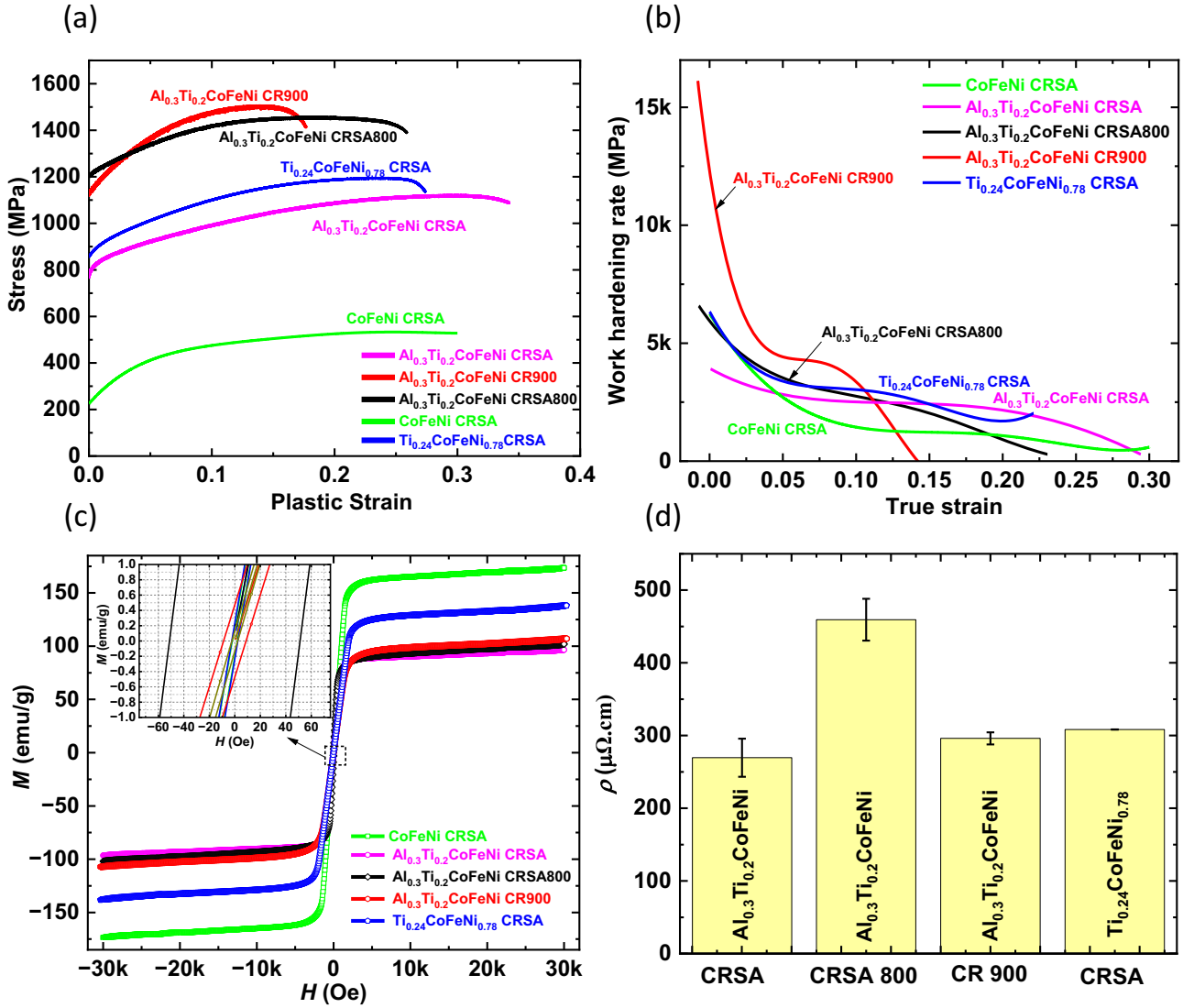

Fig. 2 | Mechanical behavior and magnetization as a function of applied magnetic field, and electrical resistivities, measured at room temperature of the solutionized CoFeNi, together with CRSA, CRSA800, and CR900 conditions of $Al_{0.3}Ti_{0.2}CoFeNi$ and $Ti_{0.24}CoFeNi_{0.78}$ HEAs. a Room temperature tensile stress-strain curves of solutionized and quenched CoFeNi, together with CRSA of $Ti_{0.24}CoFeNi_{0.78}$ and CRSA, CRSA800, and CR900 of $Al_{0.3}Ti_{0.2}CoFeNi$ and $Ti_{0.24}CoFeNi_{0.78}$ HEAs, where the CRSA condition of CoFeNi showed the lowest strength and the CR900 condition of $Al_{0.3}Ti_{0.2}CoFeNi$ showed the highest strength, **b** the corresponding work-hardening curves. **c M** versus **H** plots for the base ternary CoFeNi, and (CRSA, CRSA800, and CR900) $Al_{0.3}Ti_{0.2}CoFeNi$ and $Ti_{0.24}CoFeNi_{0.78}$ alloys, while the inset shows the magnified portion of the curves near the origin (**H** = 0 and **M** = 0), highlighting the evolution of H_c, and **d** histogram displaying the electrical resistivities for the abovementioned alloy conditions. Source data are provided as a Source Data file.

typical strength–ductility trade-off. Prior studies have shown that while CoFeNi deforms through homogeneous dislocation-mediated plasticity, the incorporation of Al and Ti in 3d transition-metal HEAs promotes planar slip, enabling sustained work hardening and enhanced ductility[49].

The corresponding work-hardening responses for CoFeNi, $Ti_{0.24}CoFeNi_{0.78}$, and the three conditions of $Al_{0.3}Ti_{0.2}CoFeNi$ (CRSA, CRSA800, CR900) are presented in Fig. 2b, further illustrating the role of compositional and processing modifications in tailoring the strength–ductility balance.

Magnetic properties and electrical resistivity measurements. Figure 2c presents the room temperature magnetization (**M**) vs applied magnetic field (**H**) curves for the base CoFeNi alloy, the $Al_{0.3}Ti_{0.2}CoFeNi$ HEA under three processing conditions (CRSA, CRSA800, CR900), and the $Ti_{0.24}CoFeNi_{0.78}$ alloy in the CRSA condition. All samples display typical soft-ferromagnetic behavior. To highlight coercivity evolution, a magnified view of the curves near the origin (**H** = 0, **M** = 0) is shown as an inset. M_s and H_c values are extracted from the curves and summarized in Table 1.

Relative to CoFeNi, the $Al_{0.3}Ti_{0.2}CoFeNi$ HEA exhibits a markedly reduced M_s of ~100 emu/g across all conditions, representing ~70% lower magnetization. While this value is significantly below conventional soft magnetic alloys like Fe–Si or Fe–Co (>180 emu/g), it is comparable to the values of Ni–Fe-based soft magnets (particularly when compared with commercial Ni-20 wt.% Fe permalloy (82 emu/g) and Ni-15 wt.% Fe-5wt.% Mo supermalloy (~70 emu/g))[9,50] and in line with other high-strength HEAs[7,43,51,52]. Importantly, the newly developed $Ti_{0.24}CoFeNi_{0.78}$ alloy demonstrates a superior property balance, achieving M_s = 137.3 emu/g together with H_c = 1.8 Oe, thereby narrowing the gap toward conventional soft magnetic materials.

The coercivity of $Al_{8.5}Ti_{5.7}Co_{28.5}Fe_{28.5}Ni_{28.}$ varies strongly with processing conditions. In the CRSA state, the alloy shows a promising H_c ~ 2.4 Oe, close to the 2.0 Oe of base CoFeNi. Upon annealing at

Table 1 | Evaluated physical (magnetic, electrical resistivity) and mechanical properties of the investigated alloys

Alloy	Condition	M_s(emu/g)	H_c(Oe)	ρ (μΩ.cm)	YS (MPa)	UTS (MPa)	Failure strain (%)
CoFeNi	CRSA	173.5	1.98	24.0[53]	275	530	33
$Al_{0.3}Ti_{0.2}CoFeNi$	CRSA	96.5	2.40	269.5 ± 26.2	780	1110	35
	CRSA800	102.0	48.63	459.3 ± 28.8	1200	1420	25
	CR900	107.6	8.8	296.1 ± 8.3	1140	1500	18
$Ti_{0.24}CoFeNi_{0.78}$	CRSA	137.3	1.8	308.3 ± 0.1	850	1200	29

800 °C (CRSA800), H_c increases substantially to ~48.8 Oe. The CR900 condition yields an intermediate H_c of ~8.8 Oe. Thus, the $Al_{0.3}Ti_{0.2}CoFeNi$ offers better soft magnetic properties in the CRSA condition rather than in the CRSA800 condition.

Figure 2d presents the corresponding electrical resistivity values. All alloy states− $Al_{0.3}Ti_{0.2}CoFeNi$ (CRSA, CRSA800, CR900) and $Ti_{0.24}CoFeNi_{0.78}$ (CRSA)−exhibit markedly higher resistivities compared to conventional soft magnetic alloys[7,9], a highly desirable feature for minimizing eddy current losses. Notably, alloying with Al and Ti increases resistivity by several fold relative to the base CoFeNi alloy (24.0 μΩ·cm)[53]. These properties are favorable compared to the recently developed $Fe_{34.51}Co_{30.32}Ni_{30.23}Ta_{4.94}$ alloy, which, despite exhibiting a lower coercivity of 4.52 Oe, possesses a significantly lower resistivity of 62.5 μΩ·cm[51,52,54]. This combination of high resistivity and low-to-moderate coercivity provides a compelling pathway for developing HEA-based soft magnets that can simultaneously address eddy current suppression and the ability to experience higher stresses in service.

Microstructural characterization

$Al_{0.3}Ti_{0.2}CoFeNi$ alloy

Solutionized and quenched sample. The nanoscale features of the $Al_{0.3}Ti_{0.2}CoFeNi$ alloy in the CRSA condition were examined using TEM and APT. Figure 3a and b present selected area electron diffraction patterns (SAEDPs), recorded along the <001> and <112> FCC zone axes, respectively. In addition to the fundamental FCC reflections, extra spots were observed at {001} positions, providing clear evidence of $L1_2$-type ordering. A corresponding dark-field image (Fig. 3c) reveals a homogeneous distribution of ~10 nm $L1_2$ precipitates embedded within the FCC matrix. High-resolution TEM (Fig. 3d) further confirms the atomic-scale structure of the FCC matrix and the ordered $L1_2$ phase.

These observations establish that the alloy exhibits a two-phase FCC + $L1_2$ microstructure even after solution annealing and quenching. This is consistent with the thermodynamic predictions and suggests that $L1_2$ nanoprecipitates form during cooling, most likely driven by the large negative enthalpies of mixing of Al and Ti with Ni, Co, and Fe.

Atom probe tomography (APT) analysis of the $Al_{0.3}Ti_{0.2}CoFeNi$ alloy in the CRSA condition further confirmed the presence of nanoscale $L1_2$ precipitates within the FCC matrix. A Ni iso-concentration surface (green color surface in Fig. 3e) constructed at a 35 at.% threshold (Fig. 3e) delineates the precipitates, revealing their nearly spherical morphology and uniform distribution within the Co–Fe–rich FCC matrix. For clarity, a 10 nm thick slice of the reconstructed volume is shown.

The compositional partitioning across the FCC/$L1_2$ interface is highlighted in the proximity histogram profiles presented in Fig. 3f. The FCC matrix exhibits an average composition of 8.2Al–4.3Ti–30.4Co–33.8Fe–23.3Ni (at.%), whereas the $L1_2$ precipitates are enriched in Ni and Ti, with a representative composition of 9.6Al–13.9Ti–26.2Co–12Fe–38.3Ni (at.%). This strong Ni–Ti enrichment supports their identification as ordered $L1_2$ precipitates.

Quantitative analysis yields an average spherical-equivalent precipitate diameter of 11.5 ± 2.2 nm and a number density of 1.24×10^{23}/m^3. The size measurement, derived from the enclosed precipitate volume, may include minor uncertainties associated with iso-concentration threshold selection. Similarly, number density estimates were corrected by assigning half-weight to precipitates intersecting the dataset boundaries.

Together with TEM, these APT observations establish that the solution-annealed and quenched $Al_{0.3}Ti_{0.2}CoFeNi$ alloy retains a finely dispersed FCC + $L1_2$ microstructure.

CRSA800 condition. A representative SEM backscattered electron (BSE) image of the $Al_{0.3}Ti_{0.2}CoFeNi$ CRSA800 sample is shown in Fig. 4a, while the corresponding electron backscatter diffraction (EBSD) phase and inverse pole figure (IPF) maps are presented in Figs. 4c and 4e, respectively. Based on EBSD analysis, the average FCC grain size of this sample was determined to be ~73 μm. A higher-magnification BSE image (Fig. 4b) reveals the presence of BCC/B2 precipitates, preferentially located at FCC grain boundaries and triple junctions. The associated EBSD phase and IPF maps in Fig. 4d and f confirms these observations.

Further microstructural details are revealed in Fig. 4g, where a high-resolution SEM image from within an FCC grain clearly shows fine nanometer-scale precipitates. The presence of $L1_2$ ordering within the FCC matrix is confirmed by the selected area diffraction pattern in the inset in Fig. 4g, recorded along the [011] FCC zone axis, which exhibits distinct (100)-type superlattice reflections. APT results from the CRSA800 condition are shown in Figs. 4h, i. Here, a 10-nm slice of the reconstructed APT volume is shown, with a Ni iso-concentration surface (green color surface in Fig. 4h) constructed at 28.5 at.% to delineate the Ni-rich $L1_2$ precipitates within the Co–Fe-rich FCC matrix. Comparison of Fig. 4h with Fig. 3e indicates that annealing at 800 °C for 4 h promoted significant growth and coarsening of the ordered $L1_2$ precipitates.

The chemical partitioning across the FCC/$L1_2$ interface was quantified using proximity histogram analysis, shown in Fig. 4i. The average compositions of the FCC matrix and $L1_2$ precipitates were measured as 8.1Al–2.9Ti–31Co–38.9Fe–19.1Ni (at.%) and 10.1Al–14.5Ti–23.7Co–9.8Fe–41.9Ni (at.%), respectively. The average spherical-equivalent diameter and number density of the $L1_2$ precipitates were determined as 27 ± 5.1 nm and 5.76×10^{21}/m^3, respectively.

Interestingly, while the compositions of the $L1_2$ precipitates and the FCC matrix remain largely unchanged compared to the solution-annealed and quenched condition, the precipitate size more than doubles, accompanied by a reduction in number density by nearly two orders of magnitude. Importantly, this significant change in precipitate size and distribution is expected to strongly influence the mechanical response of the HEA, particularly its H_c behavior, as will be discussed in a later section of this paper.

CR900 condition. To further tailor the microstructure, a different thermo-mechanical processing strategy was applied to the $Al_{0.3}Ti_{0.2}CoFeNi$ HEA. Following homogenization at 1200 °C, the alloy was cold-rolled to 90% thickness reduction and subsequently annealed directly at 900 °C for 4 h (hereafter referred to as CR900). According

https://doi.org/10.1038/s41467-026-68891-6

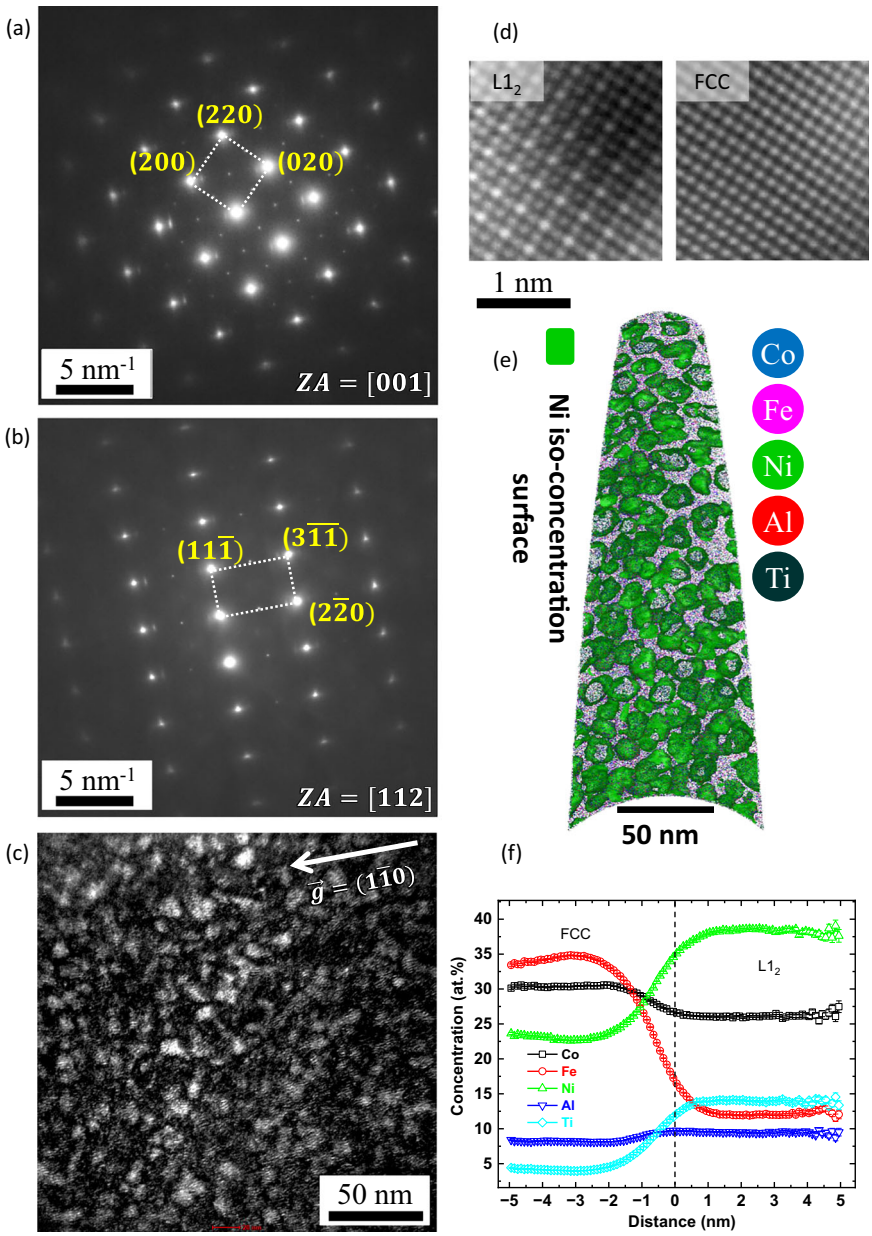

Fig. 3 | Characterization and quantification of the nano-scale phases in CRSA $Al_{0.3}Ti_{0.2}CoFeNi$ HEA. SAEDPs along **a** <001>, **b** <112> zone axes, **c** a dark-field image from a {100} superlattice reflection in (**a**) showing a homogenous distribution of $L1_2$ precipitates, **d** high-resolution TEM images showing the lattice structure of the ordered $L1_2$ precipitate and the FCC solid solution matrix, **e** Uniform distribution of $L1_2$ precipitates delineated from the FCC matrix by constructing Ni iso-concentration surface with threshold 35 at.%, a 10-nm-thick slice of the 3D reconstructed volume is presented, and **f** Corresponding chemical composition profiles (as obtained from proximity histogram analysis) for all the elements across the FCC/$L1_2$ interfaces. Source data are provided as a Source Data file.

to phase stability calculations (Fig. 1), this composition is predicted to form a stable three-phase microstructure consisting of FCC, B2, and $L1_2$ phases at 900 °C. However, as established in prior studies on FCC-based HEAs, the nucleation of the B2 phase is hindered owing to its high nucleation barrier, whereas the ordered $L1_2$ phase nucleates more readily due to a much lower barrier, due to the low FCC/ $L1_2$ interfacial energy. Consequently, B2 precipitates typically form only heterogeneously at defects such as grain boundaries and triple junctions, unlike the more uniformly distributed $L1_2$ precipitates.

The microstructure of the CR900 condition is presented in Fig. 5. A low-magnification SEM backscattered electron image (Fig. 5a), together with EBSD phase and IPF maps (Fig. 5b, c) reveal a refined FCC grain size of ~5 μm. This represents a substantial reduction compared to the cold-rolled + homogenized + quenched condition, where the FCC grains coarsened to ~73 μm. In addition to the refined FCC grains, a secondary population of BCC/B2 precipitates with an average size of ~1 μm was observed preferentially decorating FCC grain boundaries and triple junctions. The corresponding area fraction of these precipitates was ~5%.

Higher-magnification SEM-EBSD maps (Fig. 5d–f) confirmed that these boundary-associated precipitates were indexed as BCC in EBSD, consistent with the crystallographic symmetry of B2 ordering. Notably, the backscattered electron image (Fig. 5d) also revealed a finer dispersion of intragranular precipitates, which indexed as FCC in EBSD but are likely $L1_2$ ordered precipitates, since EBSD cannot differentiate between chemically ordered and disordered FCC structures.

The presence of B2 precipitates was further verified by TEM (Fig. 6). A representative bright-field TEM micrograph (Fig. 6a) shows a precipitate circled for reference, with the associated [001] BCC diffraction pattern (Fig. 6b) exhibiting (010) superlattice reflections,

https://doi.org/10.1038/s41467-026-68891-6

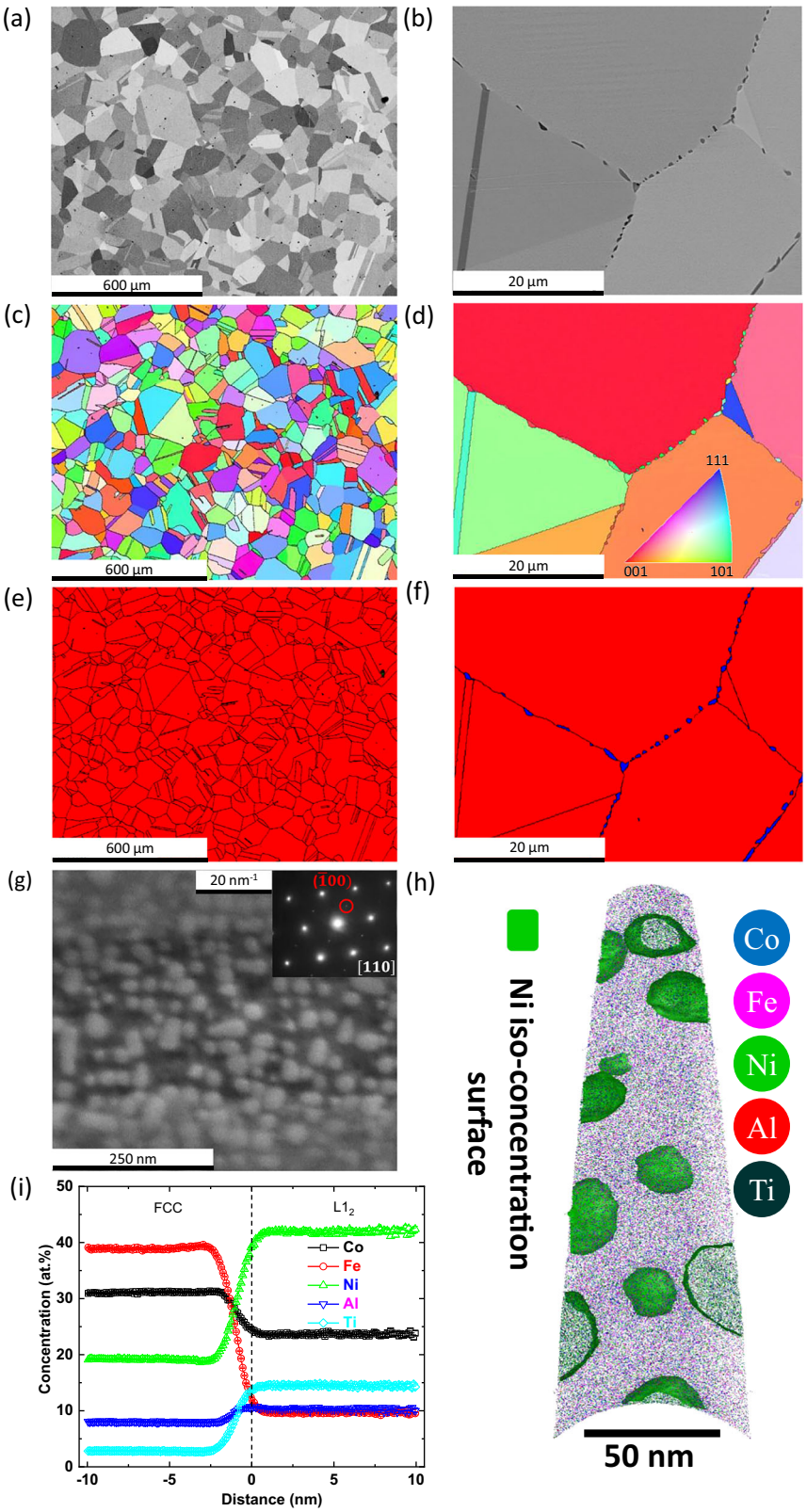

confirming B2 ordering. Dark-field imaging using the $(\bar{1}00)$ superlattice reflection (Fig. 6c) highlighted the ordered domains. A HAADF-STEM image (Fig. 6d) and elemental EDS maps (Fig. 6e–h) revealed strong partitioning of Al to the B2 phase, accompanied by enrichment of Ti and depletion of Fe. Interestingly, the Ti map also showed enrichment in numerous smaller intragranular precipitates within the FCC grains. These features were simultaneously Ni-rich and Fe-depleted, consistent with $L1_2$ precipitates.

Further evidence for intragranular $L1_2$ ordering was obtained by TEM and APT. A selected area diffraction pattern recorded along the [112] FCC zone axis (Fig. 7a) displayed distinct (110)-type superlattice reflections, indicative of $L1_2$ ordering. Complementary APT analysis

https://doi.org/10.1038/s41467-026-68891-6

Fig. 4 | Characterization and quantification of the nano-scale phases in CRSA800 $Al_{0.3}Ti_{0.2}CoFeNi$ HEA. a Low-magnification SEM backscatter image from the CRSA800 sample showing coarse FCC grains. Corresponding EBSD IPF and phase maps are shown in (**c**) and (**e**), respectively, while **b** higher-magnification SEM backscatter image from the CRSA800 sample, clearly showing BCC/B2 precipitates at the FCC grain boundaries. Corresponding EBSD IPF and phase maps are shown in (**d**) and (**f**), respectively. Note that the BCC phase is represented in blue and the FCC phase is in red. **g** High magnification backscattered electron SEM image from within a single FCC grain in the CRSA800 condition, revealing the presence of fine nanometer-scale γ′/$L1_2$ precipitates and the inset shows the TEM diffraction pattern, recorded along the [011] FCC zone axis, clearly showing the presence of (100) $L1_2$ superlattice reflections, confirming the presence of ordered precipitates within the FCC matrix grains. **h** A 10-nm-thick slice of the 3D reconstructed APT volume, showing $L1_2$ precipitates delineated by constructing a Ni iso-concentration surface with a threshold value of 28.5 at.% in the FCC matrix for the CRSA800. Note the substantially larger ordered $L1_2$ precipitates in this case as compared to the CRSA condition, and **i** corresponding chemical compositional profiles (as obtained from proximity histogram analysis) for all the elements across the FCC/$L1_2$ interfaces. Source data are provided as a Source Data file.

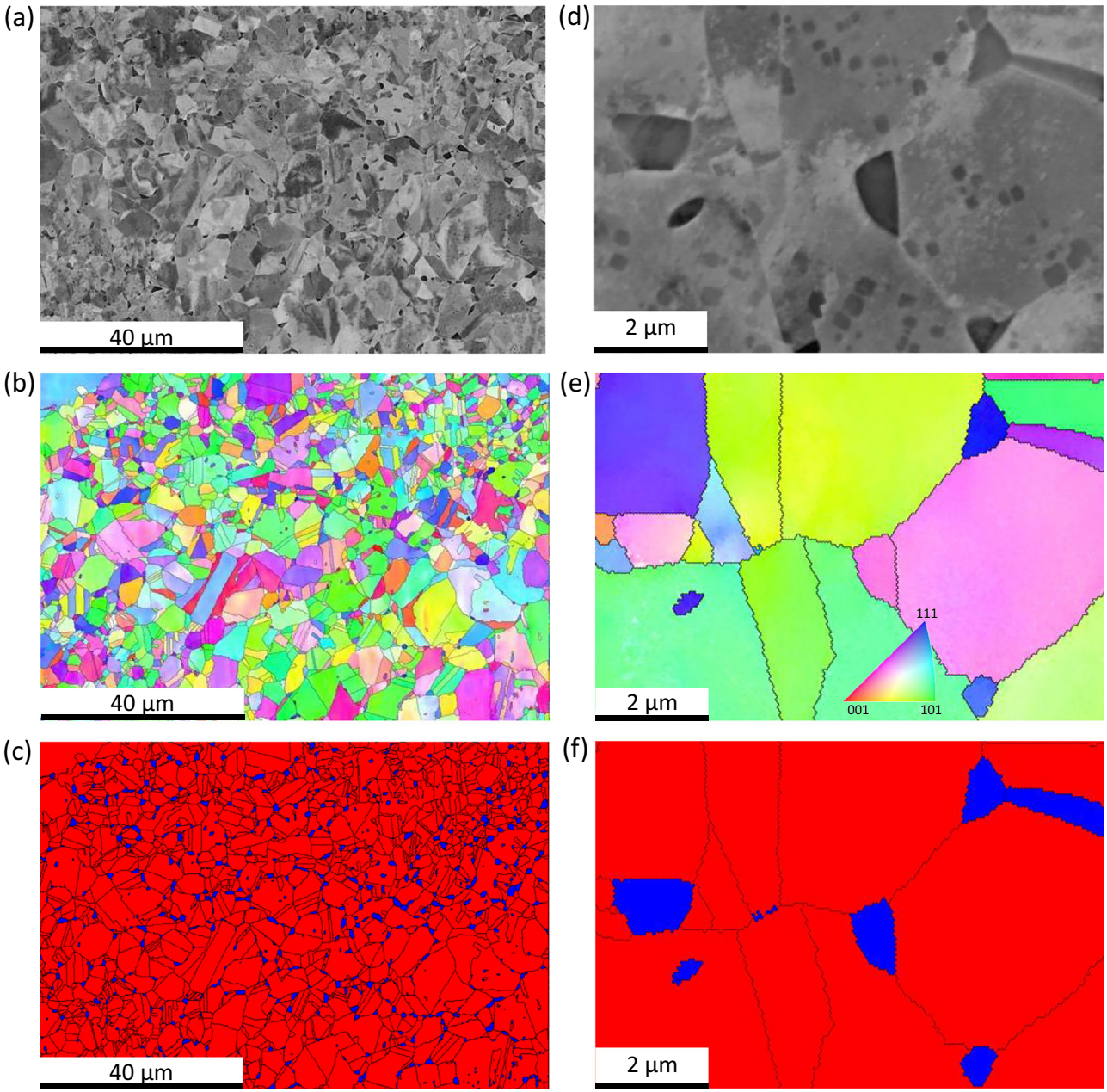

Fig. 5 | Microstructural investigation of the CRSA900 $Al_{0.3}Ti_{0.2}CoFeNi$ HEA. a Low-magnification SEM backscatter image, **b** corresponding EBSD IPF map and **c** corresponding EBSD phase maps showing FCC grains and fine scale BCC/B2 precipitates at the grain boundaries, from the same region. **d** Higher-magnification SEM backscatter image showing dark contrast BCC/B2 precipitates at the FCC grain boundaries and triple junctions, as well as nanometer-scale precipitates within the grains **e** corresponding EBSD IPF maps from the same region, and **f** corresponding EBSD phase map showing only the FCC grains and BCC/B2 precipitates. Note that the additional fine-scale intragranular precipitates are indexed as FCC and the BCC phase is represented in blue, and the FCC phase is in red. Source data are provided as a Source Data file.

https://doi.org/10.1038/s41467-026-68891-6

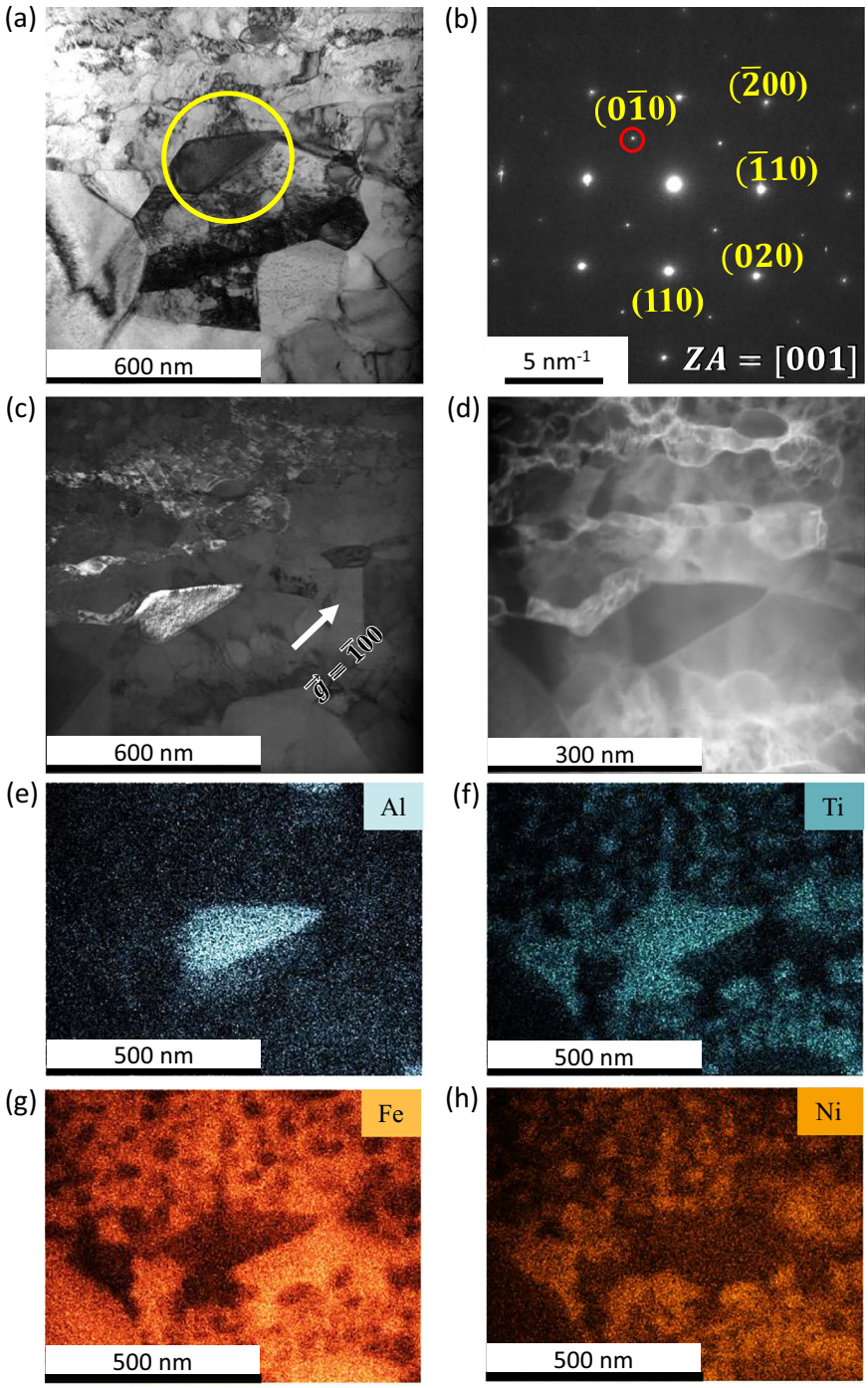

Fig. 6 | Detailed TEM analyses of the CR900 condition of $Al_{0.3}Ti_{0.2}CoFeNi$ HEA. **a** Bright-field TEM image of a B2 precipitate (marked by a yellow circle), **b** corresponding [001] BCC zone axis diffraction pattern showing (010) superlattice reflections confirming the B2 ordering within the precipitate, **c** dark-field TEM image recorded using the $(\bar{1}00)$ superlattice reflection in a two-beam condition, **d** HAADF-STEM image from the same region of the CR900 sample, corresponding elemental maps for **e** Al, **f** Ti, **g** Fe, and **h** Ni showing strong partitioning of Al to the B2 phase, accompanied by enrichment of Ti and depletion of Fe. Source data are provided as a Source Data file.

provided three-dimensional compositional mapping of the CR900 microstructure (Fig. 7b). Ni-rich $L1_2$ precipitates were identified by constructing 28.5 at.% Ni iso-concentration surfaces (green color surface), which clearly delineated the precipitates from the Fe–Co-rich FCC matrix. The number density of the $L1_2$ precipitates is evaluated as 3.4×10^{21}/m. The contribution of the precipitates in calculating the number density is considered as half, as none of the precipitates are found to be totally confined within the reconstructed volume. Further, proximity histogram analysis across the FCC/$L1_2$ interface (Fig. 7c) quantified the compositional partitioning: the FCC matrix contained ~7.1Al–3.7Ti–31.6Co–37.4Fe–20.1Ni (at.%), while the $L1_2$ precipitates were enriched in Ni and Ti (~ 8.7Al–15.7Ti–24.6Co–9.9Fe–41.1Ni, at.%).

These results establish that direct annealing at 900 °C after 90% cold rolling produces a refined FCC matrix with ~5 μm grains, decorated by B2 precipitates at boundaries and a uniform dispersion of Ni- and Ti-rich $L1_2$ precipitates within grains. The dual presence of boundary-associated B2 and intragranular $L1_2$ phases highlights the distinct nucleation pathways of the two ordered structures:

https://doi.org/10.1038/s41467-026-68891-6

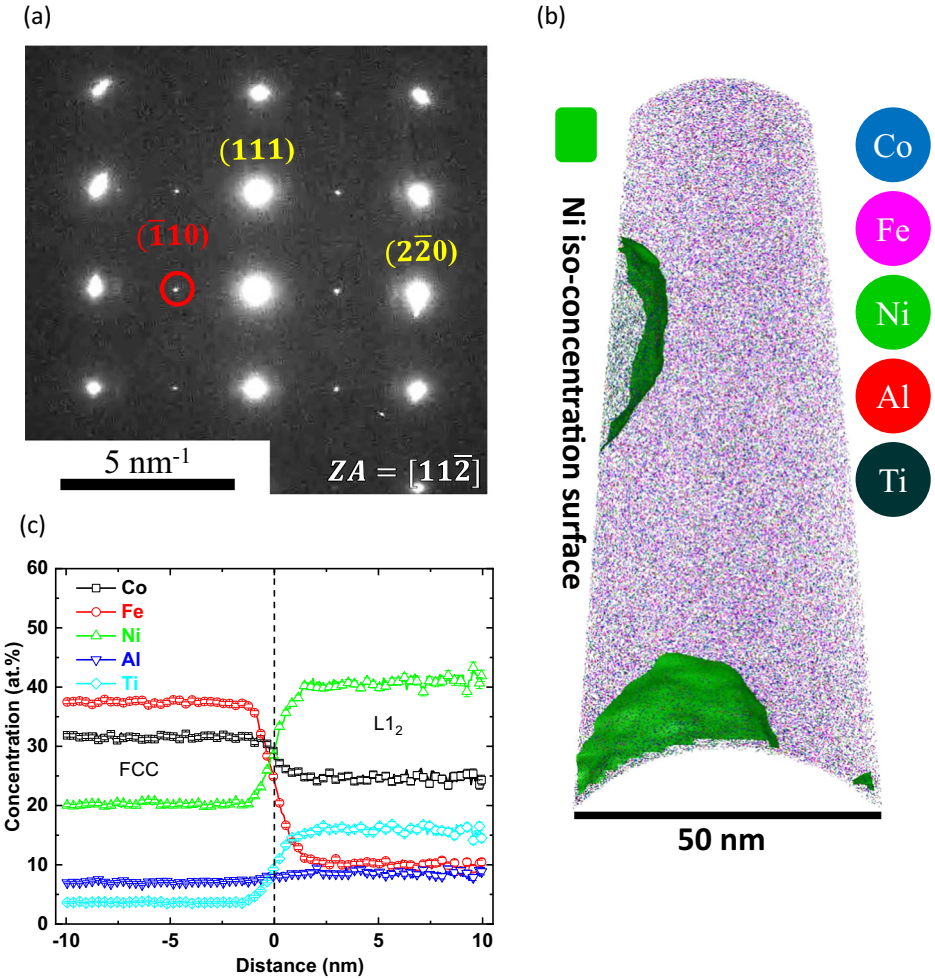

Fig. 7 | Characterization and quantification of the nano-scale phases in CR900 $Al_{0.3}Ti_{0.2}CoFeNi$ HEA. a TEM diffraction pattern, recorded along a [112] FCC zone axis revealing (110) superlattice reflections arising from the fine-scale $L1_2$ precipitates within the FCC grains, as seen in the SEM image in Fig. 5d, **b** a 10-nm-thick slice of the 3D reconstructed APT volume, showing $L1_2$ precipitates delineated by constructing Ni iso-concentration surface with threshold value of 28.5 at.% in the FCC matrix for the CR900, and **c** chemical compositional profiles for all the constituent elements across the FCC/$L1_2$ interfaces, showing enrichment of Ni and Ti in the $L1_2$ precipitate. Source data are provided as a Source Data file.

heterogeneous for B2 and homogeneous for $L1_2$. This microstructural configuration is expected to significantly influence the mechanical response of the alloy by combining grain refinement with multi-scale precipitation strengthening.

$Ti_{0.24}CoFeNi_{0.78}$ alloy

Figure 8 presents the microstructural characterization of the $Ti_{0.24}CoFeNi_{0.78}$ alloy in its solution-annealed condition. EBSD analysis (Fig. 8a) revealed an equiaxed FCC grain structure with an average grain size of 100 ± 25.6 μm. High-resolution SEM imaging in the back-scattered mode (Fig. 8b) showed the presence of nanoscale precipitates, which were further confirmed by dark-field TEM (Fig. 8c). SAEDPs recorded along the <011> BCC zone axis (Fig. 8d) displayed additional {001} and {011} reflections, unambiguously establishing the presence of $L1_2$ ordering within the FCC matrix.

Interestingly, despite undergoing solution annealing and subsequent quenching, the alloy retained a dual-phase FCC + $L1_2$ microstructure. This indicates that $L1_2$ precipitates homogeneously nucleated during cooling, most likely facilitated by the large negative enthalpy of mixing between Ti and Ni/Co/Fe, which promotes ordering. APT provided further insight into the chemical partitioning behavior. Ti atom maps from a 10-nm slice of the reconstructed volume (Fig. 8e) highlighted pronounced Ti partitioning, with $L1_2$ precipitates clearly delineated through a Ti iso-concentration surface (black color surface) at a threshold of 15 at.%.

Compositional analysis across the FCC/$L1_2$ interface, obtained from proximity histogram profiles (Fig. 8f), revealed distinct partitioning of alloying elements. The average composition of the FCC matrix was 2.5Ti-34.0Co-44.4Fe-19.0Ni (at.%), whereas the $L1_2$ precipitates were significantly enriched in Ti and Ni, with an average composition of 23.6Ti-27.6Co-7.3Fe-41.5Ni (at.%). Quantitative analysis of the precipitate population showed an average spherical-equivalent diameter of 4.0 ± 0.8 nm and a number density of $6.29 \times 10^{23}/m^3$.

These results confirm that, even under solution-annealed and quenched conditions, the $Ti_{0.24}CoFeNi_{0.78}$ alloy exhibits a stable two-phase FCC + $L1_2$ microstructure, driven by strong chemical partitioning and ordering tendencies.

Discussion

The present study demonstrates a novel strategy for the design of high-strength, soft magnetic, and high resistivity HEAs by carefully tuning composition and processing pathways to control nanoscale precipitation behavior. Specifically, Ti and Al additions to the equiatomic CoFeNi alloy promote the formation of ordered $L1_2$ precipitates within an FCC matrix, thereby achieving a remarkable balance between strength, ductility, electrical resistivity, and soft magnetic properties.

https://doi.org/10.1038/s41467-026-68891-6

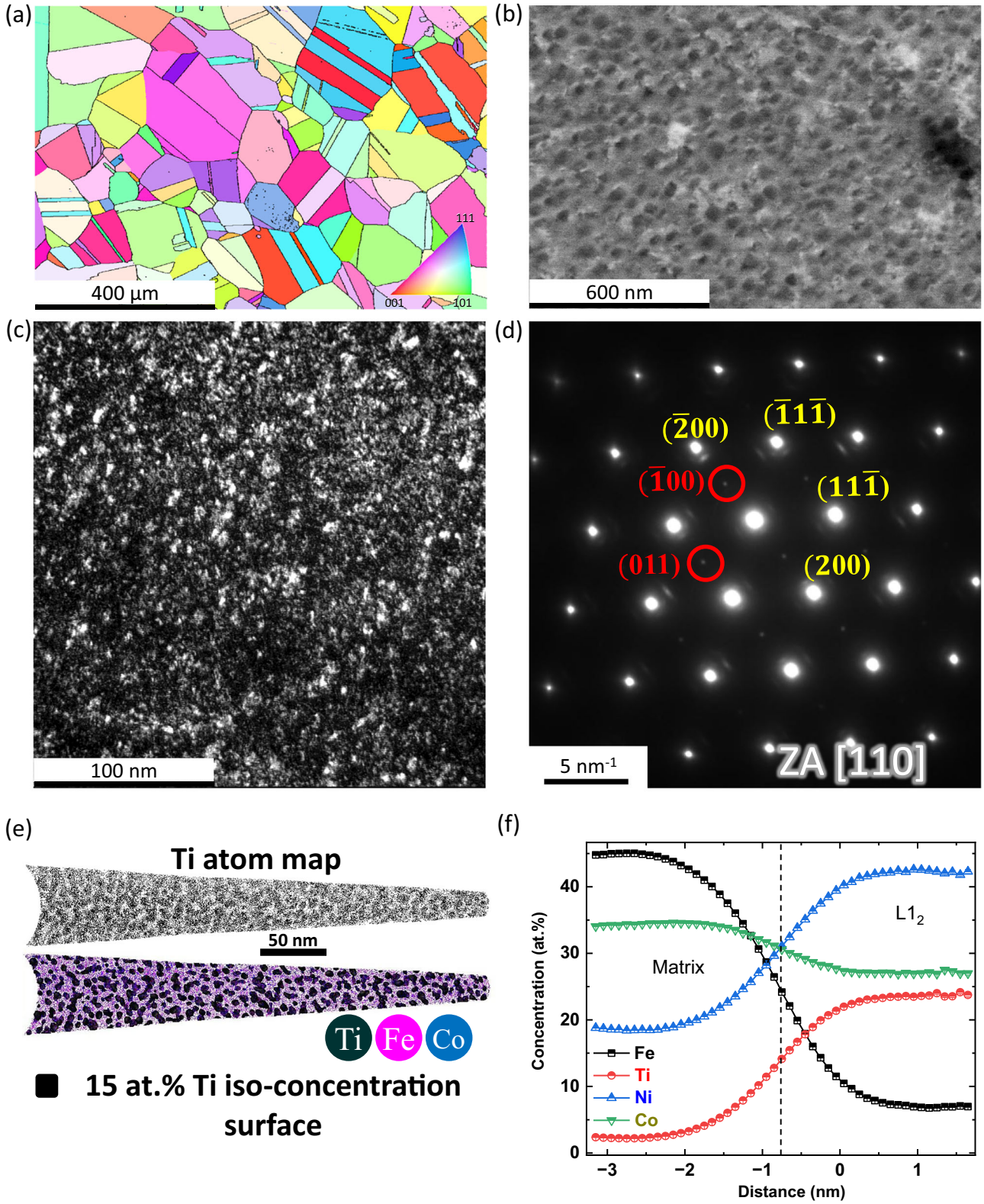

Fig. 8 | Characterization and quantification of the nano-scale phases in $Ti_{0.24}CoFeNi_{0.78}$ alloy. a An IPF-Z map of the microstructure of the $Ti_{0.24}CoFeNi_{0.78}$ alloy. **b** A BSE micrograph showing the fine-scale $L1_2$ precipitates. **c** A dark-field TEM micrograph showing the $L1_2$ precipitates. **d** SAEDPs recorded along the <011> BCC zone axis, showing additional {001} and {011} reflections from the ordered $L1_2$ precipitates. A 10-nm-thick slice of the 3D reconstructed APT analysis volume displaying **e** Ti atom map (top), and the Fe and Co atom maps superimposed with 15 at.% Ti iso-concentration surface (bottom) clearly confirms the presence of nano-scale Ti-rich $L1_2$ precipitates, and **f** the corresponding chemical concentration profiles for all the constituent elements present in the alloy across the FCC/$L1_2$ interfaces. Source data are provided as a Source Data file.

Primarily, two distinct HEA compositions have been designed in this study, $Al_{0.3}Ti_{0.2}CoFeNi$ and $Ti_{0.24}CoFeNi_{0.78}$, to exploit the effectiveness of ordered $L1_2$ precipitates in enhancing the mechanical properties, while maintaining the soft magnetic behavior. In this context, the formation of the ordered $L1_2$ precipitates within the random solid solution FCC parent matrix in the case of both $Al_{0.3}Ti_{0.2}CoFeNi$ and $Ti_{0.24}CoFeNi_{0.78}$ HEAs occurs via a nucleation and growth process. At the earliest stage of this phase transformation, nucleation of nanometer-scale ordered $L1_2$ domains takes place within the parent FCC matrix. These ordered $L1_2$ domains are likely to be fully coherent with the parent FCC matrix and therefore do not exhibit any substantial difference in the lattice parameter. Rather, these ordered $L1_2$ domains are early stages of the second phase exhibiting a distinctly different composition and chemical ordering, as compared to the FCC matrix, which is a random solid solution. This corresponds to the CRSA condition for both HEAs and is manifested as superlattice reflections in the electron (refer to Fig. 3a, b, and Fig. 8d) and X-ray (refer to Fig. S1) diffraction patterns and compositional differences highlighted in the APT results (refer to Fig. 3e, f, and Fig. 8e, f). Further, the distinctly ordered domains are clearly highlighted in the dark-field images shown in Fig. 3c and Fig. 8c, recorded using the {001} type superlattice reflection of the ordered $L1_2$ phase. However, the XRD patterns for both investigated alloys under the CRSA condition show no discernible splitting of the characteristic FCC peaks. This is because the lattice parameters of the FCC and $L1_2$ phases are not substantially different at this early stage. Upon further annealing of these quenched HEAs, in case of the CRSA800 and CR900 conditions of the $Al_{0.3}Ti_{0.2}CoFeNi$ HEA, there is growth and coarsening of the ordered $L1_2$ precipitates, leading to larger differences in lattice parameters, and eventual loss of coherency between the $L1_2$ precipitate and the FCC matrix, and consequently, splits appear in the XRD peaks.

Coarsening and coherency loss of $L1_2$ precipitates directly govern the alloy's mechanical and magnetic response. Considering the effective control over precipitation and resulting properties, these results highlight a design paradigm for cost-effective, Ta-free HEAs that rival or surpass state-of-the-art Ta-containing HEAs, and conventional commercial soft magnetic alloys, in terms of the balance of soft magnetic properties, mechanical response, and resistivity.

Precipitation-mediated strengthening and property enhancement

The precipitation of nanoscale $L1_2$ phases is central to the superior mechanical and physical performance of the investigated alloys. In the $Ti_{0.24}CoFeNi_{0.78}$ alloy, the formation of ultrafine (~ 4.0 nm), uniformly distributed $L1_2$ precipitates at extremely high number densities (6.29×10^{23} /m^3) provides significant strengthening by interacting with dislocations during plastic deformation. Despite such dense precipitation, the small precipitate size ensures minimal pinning of magnetic domain walls, resulting in very low coercivity (~ 1.8 Oe). The concurrent enhancement in yield strength (YS ~ 850 MPa), ultimate tensile strength (UTS ~ 1200 MPa), ductility (~ 29%), and resistivity (308.3 μΩ·cm), while retaining a high saturation magnetization (137.3 emu/g), positions this alloy among the best-performing soft magnetic alloys reported to date. By contrast, in the $Al_{0.3}Ti_{0.2}CoFeNi$ alloy, larger $L1_2$ precipitates (~ 11.5 nm) form at lower number densities (1.24×10^{23} /m^3). While the mechanical response remains impressive (YS ~ 780 MPa, UTS ~ 1110 MPa, elongation ~35%), the saturation magnetization decreases substantially (~ 96.5 emu/g) due to compositional partitioning, and the coercivity increases modestly (~ 2.4 Oe).

$L1_2$ crystal structure is based on an ordered FCC superlattice, which often leads to the precipitation of the γ′ Ni_3(Al, Ti) phase in Ni-based superalloys. The low lattice misfit between the coherent ordered γ′ precipitates and the disordered FCC matrix minimizes interfacial energy, resulting in a low nucleation barrier. Therefore, these γ′ precipitates can homogeneously nucleate in the FCC matrix, as we observe in the present study. This has been well-established in the published literature on superalloys and has a strong impact on the mechanical properties[55]. The γ′ precipitates significantly strengthen the superalloy by impeding the movement of dislocations through the crystal lattice via two main mechanisms: (i) Dislocation Shearing: smaller γ′ precipitates (typically <50 nm) get sheared by dislocations, which can be impeded due to the formation of anti-phase boundary within the precipitate, which requires energy. (ii) Orowan bowing: for larger precipitates (typically >50 nm), it is energetically more favorable for the dislocation to bend and bypass them via a bowing mechanism. The quantitative nanoscale $L1_2$ precipitate information, as obtained from APT analysis, can be utilized to get an estimate of qualitative YS information of the investigated alloys ($Ti_{0.24}CoFeNi_{0.78}$ and $Al_{0.3}Ti_{0.2}CoFeNi$) in their respective CRSA condition. According to Orowan's simplified model of precipitation strengthening[56],

$$YS \propto \sqrt{N_v D} \tag{1}$$

where N_v is the precipitate number density, and D is the diameter. Now, $Ti_{0.24}CoFeNi_{0.78}$ alloy has a higher number density (6.29×10^{23}/m^3) and a smaller diameter (4.0 ± 0.8 nm) of $L1_2$ precipitates in comparison to $Al_{0.3}Ti_{0.2}CoFeNi$ alloy (1.24×10^{23}/m^3, diameter 11.5 ± 2.2 nm) in the CRSA condition, that lead to higher YS for the alloy.

On the other hand, the evolution of coercivity depends on the interaction of magnetic domain wall movement with these γ′ precipitates. When the precipitate size is smaller than the magnetic domain wall width[43,52], it has a weaker effect on the movement of the magnetic domain wall, hence the material remains magnetically soft while providing mechanical strength. Additionally, the coherency stresses arising from the misfit between FCC and γ′ phases can further resist the domain wall motion. Within the coherency limit, the larger the size of the γ′ precipitates, the higher the coherency stresses. The experimental results presented here clearly indicate that the γ′ precipitates in the case of the solution annealed and quenched condition (CRSA) for both candidate HEAs, $Al_{0.3}Ti_{0.2}CoFeNi$ (~11.5 nm) and $Ti_{0.24}CoFeNi_{0.78}$ (~ 4.0 nm), are sufficiently small such that they offer a weak resistance to domain wall motion. In contrast, the substantially larger γ′ precipitates in the case of the 800 °C/5 h annealed (CRSA800) and 900 °C/4 h (CR900) conditions of $Al_{0.3}Ti_{0.2}CoFeNi$ result in higher values of coercivity. Similar justifications have been discussed in recent literature[24,43,52]. Further, the presence of a smaller number of non-magnetic elements (like Ti and Al), and a higher amount of Fe and Co (carries higher magnetic moments than Ni) leads to higher saturation magnetization for the $Ti_{0.24}CoFeNi_{0.78}$ alloy.

This contrast underscores how precipitate size, chemistry, and number density—governed by alloy composition—control the trade-offs between strength, ductility, resistivity, and magnetic properties. Such insights are important because they suggest routes to independently tune mechanical and magnetic properties through compositionally driven control of precipitation size, kinetics, and chemistry.

Microstructural evolution and its impact on magnetic and electrical properties

Annealing treatments further reveal how precipitate coarsening alters property balance. Growth of $L1_2$ precipitates to ~27 nm in the CRSA800 condition of $Al_{0.3}Ti_{0.2}CoFeNi$ dramatically increases strength (YS ~ 1200 MPa) but also raises coercivity nearly 20-fold (~ 48.6 Oe) due to domain wall pinning. This result illustrates the trade-offs between mechanical properties and magnetic softness: while coarser precipitates act as effective barriers to dislocation motion, they simultaneously increase magnetostatic energy and coercivity, and impede domain wall mobility, which raises coercivity and compromises soft magnetic performance.

Thermo-Calc predictions and experimental results provide additional insight. At higher annealing temperatures, the alloy stabilizes a

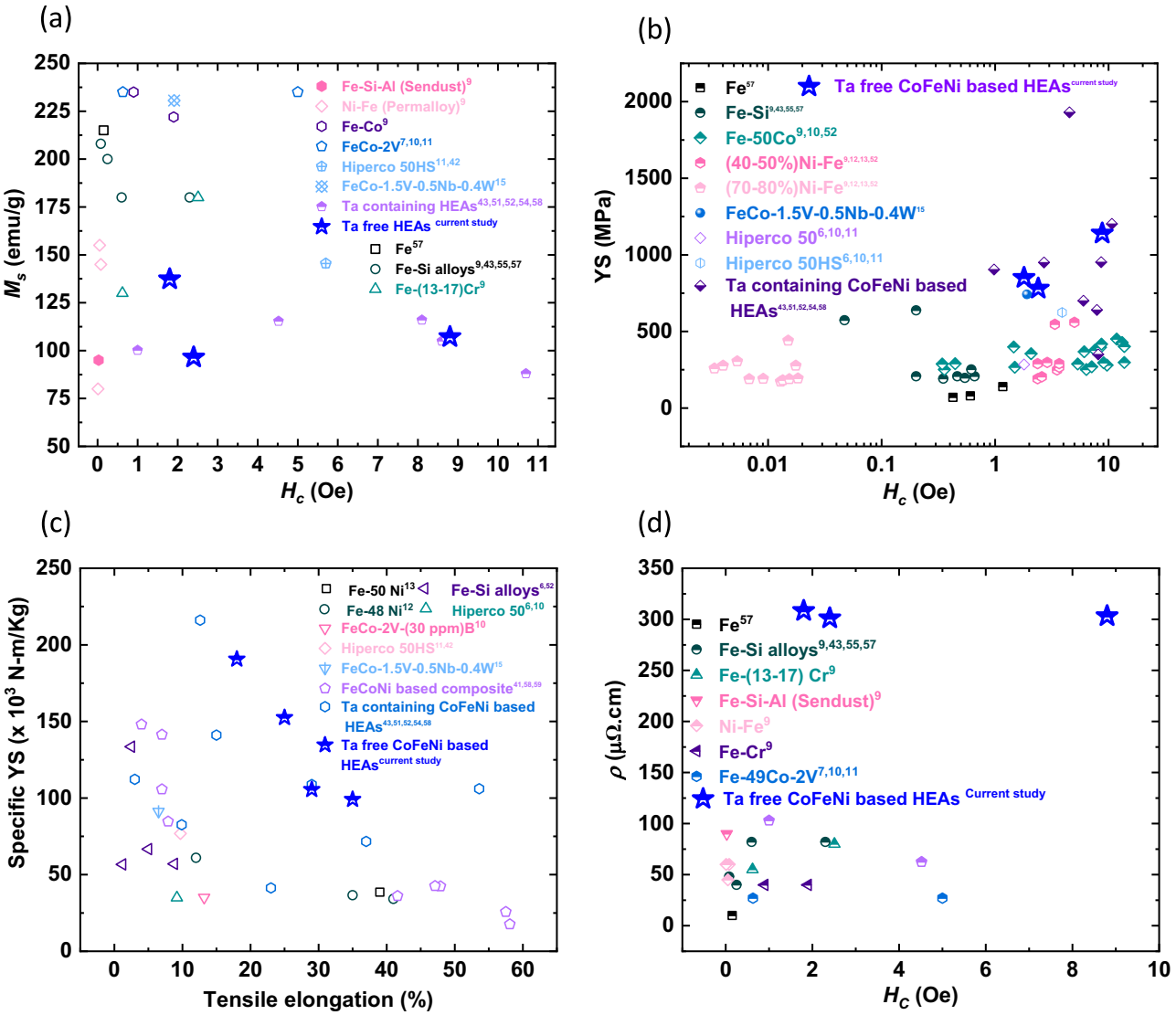

Fig. 9 | Ashby plots illustrating the unique position of the currently investigated Ta-free HEAs within the broader landscape of soft magnetic materials, consisting of both conventional and HEAs. a M_s versus H_c, **b** YS versus H_c, **c** specific YS versus tensile elongation, and **d** ρ versus H_c values. These plots compare the magnetic and mechanical properties of the currently investigated alloy with the other known high-strength soft magnetic materials, such as pure Fe[7], Fe–Si[7,9,43,55], Fe-Cr[9], Fe–Si–Al (sendust)[9],Ni–Fe (permalloy)[9], Ni–Fe–Mo (supermalloy), Fe–Co[9], Fe-49Co-2V (Hiperco)[7,10,11], Fe-49Co-2V-30ppm B[10], commercial Hiperco 50HS (Fe-49Co-1.9V-0.3 Nb)[11,42], FeCo-1.5V0.5Nb0.4W[15], Fe–Ni–Co-based composite[41,57,58] and Ta-containing FeNiCo-based HEAs[43,51,52,54,57].

minor fraction of B2 precipitates, typically nucleating heterogeneously at grain boundaries and triple junctions. These precipitates, while coarse, alter solute partitioning and reduce supersaturation within FCC grains, leading to fewer intragranular $L1_2$ precipitates. This effect is evident in the CR900 condition of $Al_{0.3}Ti_{0.2}CoFeNi$, where direct annealing after cold rolling produces a three-phase microstructure: fine FCC grains (~5 μm), ~5% B2 precipitates (~1 μm), and a small fraction of the coarse $L1_2$ precipitates (~30–50 nm). This microstructure yields a superior property combination: high YS (~1140 MPa), UTS (~1500 MPa), and good ductility (~18%), coupled with low coercivity (~8.8 Oe) and moderate M_s (~107.6 emu/g). Notably, although the strength levels are comparable to those of CRSA800, the coercivity is nearly six times lower, underscoring the critical role of microstructural pathway engineering in balancing strength and magnetic softness.

Further, the enhanced electrical resistivity for the currently investigated alloys (see Fig. 2d, Table 1, Fig. 9d) can be attributed to their high inelastic electron scattering in the distorted lattice due to the presence of nano-scale precipitates in the microstructure. Evolution of resistivity for the $Al_{0.3}Ti_{0.2}CoFeNi$ (CRSA, CRSA800, and CR900) alloy follows a similar trend to its coercivity. This suggests that the evolution of resistivity is intrinsically linked to the formation of nanoscale $L1_2$ and B2 precipitates. On the other hand, the CRSA $Ti_{0.24}CoFeNi_{0.78}$ alloy shows a slightly higher resistivity than the CRSA $Al_{0.3}Ti_{0.2}CoFeNi$ alloy. This can be attributed to the higher number density of $L1_2$ precipitates in the former, which provides more sites for electron scattering.

Mechanistic insights into strengthening

The contrasting strengthening mechanisms in CRSA800 and CR900 highlight how different microstructural features govern deformation resistance. In CRSA800, strengthening arises primarily from a dense population of coherent $L1_2$ precipitates (~27 nm), akin to γ′ precipitates in Ni/Co-based superalloys, which are shearable and impart strength without severely compromising ductility. The cutting of coherent ordered precipitates contributes to both strengthening and

ductility retention, a synergy rarely achieved in traditional commercial magnetic alloys.

By comparison, in CR900, strengthening is dominated by fine FCC grain size (~5 μm), with additional but secondary contributions from coarse B2 boundary precipitates and a small fraction of intragranular $L1_2$ phase. Grain refinement strengthens the alloy via the Hall–Petch effect, while B2 precipitates provide boundary pinning and secondary resistance to deformation. Thus, while both microstructures achieve high strength, their differing impacts on coercivity reveal distinct trade-offs between mechanical and magnetic performance. The comparison also emphasizes that different strengthening mechanisms—precipitate shearing versus grain boundary strengthening—carry different penalties or advantages for soft magnetic properties.

Magnetic domain interactions and coercivity control

The results also provide a mechanistic understanding of how nanoscale precipitates influence magnetic softness. In the CRSA condition, the $Al_{0.3}CoFeNi$ alloy contains $L1_2$ precipitates with an average size of ~11.5 nm. Since the domain wall width in such FCC–$L1_2$ microstructures has been reported to be ~171 nm (as demonstrated by Kovács et al. for a similar alloy[24]), the precipitates are substantially smaller than the domain wall width. This size mismatch minimizes domain wall–precipitate interactions, thereby maintaining low coercivity. A similar argument explains the exceptionally low coercivity (1.8 Oe) of the $Ti_{0.24}CoFeNi_{0.78}$ alloy in the CRSA condition, where the $L1_2$ precipitates are even finer (~4.0 nm) and thus impose negligible resistance to domain wall motion. In contrast, when precipitates coarsen to ~27 nm (CRSA800), the increased size produces stronger magnetostatic interactions and coherency stresses, effectively pinning domain walls and drastically raising coercivity. Here, it may be noted that pinning of the magnetic domain wall is more severe, as it has been shown that the domain wall width reduces (~35 nm) for FCC + $L1_2$ + BCC/B2 containing microstructure in a similar HEA[24]. The CR900 condition offers an intermediate solution: while grain boundaries do contribute to some pinning, the absence of a high density of coarsened intragranular $L1_2$ precipitates prevents a severe increase in coercivity. These results align with theoretical predictions and prior studies on CoFe-based alloys but extend the understanding by highlighting the role of alloy chemistry in simultaneously controlling precipitate size distribution and magnetic performance.

Comparison with other alloys

Benchmarking against commercial and literature-reported soft magnetic alloys reveals the unique positioning of the present Ta-free HEAs (see Fig. 9 and Supplementary Table 1). Conventional alloys such as Si steel, Ni–Fe permalloy, Ni–Fe–Mo supermalloy, and Fe–Co–V-based Hiperco exhibit low coercivity and high M_s but suffer from low strength and poor resistivity[7,9]. For example, Hiperco 50HS[11,14] achieves YS ~ 415-624 MPa with ~10 % ductility, but its resistivity (27–80 μΩ·cm) and coercivity (~1.8-8.0 Oe) are inadequate for emerging high-frequency, high-speed applications. Even with W additions to Hiperco 50HS enhance strength (~752 MPa) and maintain low coercivity (~1.9 Oe), these alloys lack sufficient resistivity for next-generation devices[15]. By comparison, $Ti_{0.24}CoFeNi_{0.78}$ offers YS values nearly 40% higher, along with fourfold higher resistivity, while maintaining coercivity levels well below Hiperco.

Recent developments in Ta-containing CoFeNi HEAs by Han and co-workers achieved YS values up to 1930 MPa with low coercivity (0.97–10.7 Oe) and moderate M_s (~100–115 emu/g)[51,52,54]. However, their resistivity (~106 μΩ·cm) and density are lower than desired, while the presence of expensive Ta increases cost and limits scalability. In contrast, the present Ti- and Al-modified CoFeNi HEAs achieve comparable or superior performance: CRSA $Ti_{0.24}CoFeNi_{0.78}$ combines a high strength-to-weight ratio (specific YS ~ 105.5 kN·m/kg), low H_c (1.8 Oe), high M_s (137.3 emu/g), and exceptional resistivity (308.3 μΩ·cm). Similarly, the CRSA condition of $Al_{0.3}Ti_{0.2}CoFeNi$ alloy is also competitive in terms of the balance of soft magnetic and mechanical properties, while preserving high resistivity. Additionally, the CR900 condition of the $Al_{0.3}Ti_{0.2}CoFeNi$ alloy delivers even higher strength (YS ~ 1140 MPa, UTS ~ 1500 MPa) with low coercivity (8.8 Oe) and good ductility (18%). These attributes collectively surpass Ta-containing HEAs in several key metrics while reducing density and material cost. Thus, the present alloys provide a more sustainable and competitive alternative to both conventional and advanced commercial alloys.

Technological implications for next-generation devices

The properties demonstrated in this work directly align with requirements for next-generation high-speed electrical machines, flywheel energy storage systems, and other advanced electromechanical devices. In high-speed motors, increasing rotational velocity raises centrifugal stresses that demand higher yield strength in rotor laminations. Failure to meet this requirement results in irreversible deformation, air gap variation, and reduced efficiency. The $Ti_{0.24}CoFeNi_{0.78}$ alloy, with its ultrafine precipitate architecture, offers YS ~ 850 MPa—well beyond commercial alloys—allowing stable operation at higher rpm and power densities.

Equally critical is electrical resistivity. High resistivity minimizes eddy current losses at high frequencies, a key factor in modern compact and efficient electrical devices. With resistivity exceeding 300 μΩ·cm, $Ti_{0.24}CoFeNi_{0.78}$ offers nearly an order-of-magnitude improvement over conventional alloys, ensuring reduced heat generation and enhanced efficiency. Coupled with low coercivity and high M_s, this combination minimizes hysteresis and improves induction, thereby lowering overall losses.

Moreover, ductility levels of 18–35% across the studied alloys enable forming into complex shapes, and damage tolerance under high stresses attributes rarely met simultaneously with high-strength and soft magnetic behavior. This ductility not only extends service life under dynamic conditions but also expands design possibilities for complex geometries in rotors and stators, which can optimize magnetic flux paths and torque performance.

Sustainability, cost, and scalability considerations

Another key implication of the present study lies in sustainability and economic viability. Ta is both expensive and geopolitically constrained, inhibiting applications of Ta-containing HEAs. By eliminating Ta, the present Ti- and Al-based systems reduce cost, supply risk, and embodied energy. Furthermore, their nearly 10% lower density relative to Ta-based HEAs reduces overall component mass, improving efficiency in high-speed rotating applications. These advantages are critical in transitioning advanced soft magnetic alloys from laboratory prototypes to industrial adoption. It may be noted here that the currently investigated HEAs are more expensive than the conventional Fe–Si-based SMMs. However, considering the better mechanical strength and ductility and the high electrical resistivity of the currently investigated alloys, their service life is expected to be longer. This can be reasonably expected to offset the higher anticipated processing cost of these alloys.

This study establishes a robust design pathway for high-performance soft magnetic high-entropy alloys (HEAs) through precipitation-mediated strengthening while retaining low H_c, appreciable M_s, and high resistivity in Ta-free CoFeNi-based systems. By judiciously adding Ti and Al, we demonstrate that nanoscale ordering can be harnessed to introduce a dense population of ultrafine $L1_2$ precipitates. If the length scale and distribution of these precipitates are appropriately controlled, then this simultaneously enhances mechanical strength and electrical resistivity, while preserving the soft magnetic behavior—properties that are typically difficult to achieve in conventional soft magnetic alloys.

Based on this approach, two CoFeNi-based HEAs with minor additions of Ti and/or Al have been developed: $Ti_{0.24}CoFeNi_{0.78}$ and quinary$Al_{0.3}Ti_{0.2}CoFeNi$. The rather exceptional balance of properties of these two alloys has been summarized below:

The $Ti_{0.24}CoFeNi_{0.78}$ alloy demonstrates a rare combination of low coercivity (~1.8 Oe), high saturation magnetization (~137.3 emu/g), and ultrahigh electrical resistivity (308.3 μΩ·cm). These properties are coupled with remarkable mechanical properties, including a yield strength of ~850 MPa, ultimate tensile strength of ~1200 MPa, and tensile elongation of ~29%. While state-of-the-art Ta-containing HEAs may exhibit marginally lower coercivity values, they also generally exhibit lower M_s (~100 emu/g) and much lower resistivity (62–117 μΩ·cm). Therefore, the newly proposed $Ti_{0.24}CoFeNi_{0.78}$ composition offers clear advantages for reducing eddy current losses and meeting the magnetic requirements of future electrical machines.

While the other proposed CoFeNi-based composition, the quinary$Al_{0.3}Ti_{0.2}CoFeNi$ alloy exhibits a marginally higher coercivity (~2.4 Oe) and M_s (96.5 emu/g), it provides more tunability. This alloy also combines high resistivity (~269.5 μΩ·cm) and very good mechanical properties in the cold-rolled, solutionized, and quenched (CRSA) condition (YS ~ 780 MPa, UTS ~ 1100 MPa, elongation ~30%). Controlled thermo-mechanical processing allows further property optimization: while precipitate coarsening at 800 °C boosts the YS to ~1200 MPa and UTS to ~1420 MPa, it substantially increases coercivity (~48.6 Oe). In contrast, direct annealing of the cold-rolled condition at 900 °C produces a refined three-phase microstructure with very high YS ~ 1140 MPa, UTS ~ 1500 MPa, elongation ~18%, high resistivity (296.1 μΩ·cm), and lower coercivity (~8.8 Oe), achieving an attractive balance of strength, electrical, and soft magnetic behavior.

Therefore, these newly developed CoFeNi-based HEAs offer a competing alternative to Ta-containing HEAs and surpass conventional Fe-based soft magnetic alloys, especially in terms of mechanical properties and electrical resistivity. These HEAs provide a lightweight, cost-effective, and scalable alternative for next-generation high-speed electrical machines, flywheel energy storage, and other demanding applications.

Methods

Alloy preparation and thermo-mechanical processing

$Al_{0.3}Ti_{0.2}CoFeNi$ and $Ti_{0.24}CoFeNi_{0.78}$ alloys, with nominal compositions 8.5Al–5.7Ti–28.5Co–28.5Fe–28.5Ni (at.%) and 8Ti–33Co–33Fe–26Ni (at.%), respectively, were procured from ACI Alloys Inc. The alloys were vacuum arc remelted (VAR) five times under an Ar atmosphere, with intermediate flipping, to ensure chemical homogeneity. The actual bulk compositions, measured using wavelength dispersive X-ray fluorescence spectroscopy (WDS-XRF, Rigaku Primus IV), were 6.6Ti–7.1Al–29.1Co–28.8Fe–28.4Ni (at.%) and 32.9 Co–33.4Fe–25.8Ni–7.9Ti (at.%), as shown in Supplementary file (Supplementary Table 2). An XRD experiment was carried out to investigate the crystal structure of the alloys (see Supplementary Fig. 1 and Supplementary Table 3) using a tabletop Bruker D6 Phaser instrument with Cu $K\alpha$ radiation ($\lambda = 1.54$ Å).

The cast alloys were homogenized at 1200 °C for 1 h, followed by 90% reduction in thickness through cold cross-rolling. The rolled plates were then solution annealed at 1200 °C for 5 min (encapsulated in stainless steel foil) and water-quenched to yield a single-phase FCC solid solution with an average grain size of ~190 μm. This state is referred to as the CRSA condition. A subset of $Al_{0.3}Ti_{0.2}CoFeNi$ samples was subsequently annealed at 800 °C for 4 h (CRSA800). Another set of homogenized and cold-rolled samples was annealed at 900 °C for 4 h (CR900).

Microstructural analysis

Microstructural characterization was carried out using a FEI Nova NanoSEM 230™ scanning electron microscope (SEM) and a FEI Tecnai G2 TF20™ transmission electron microscope (TEM) operated at 200 kV. SEM samples were prepared by grinding and polishing to 4000 grits, followed by final polishing in 1 μm colloidal silica using a Vibromet system. Electron backscatter diffraction (EBSD) measurements were performed on a ThermoFisher Apreo-2S scanning electron microscope (SEM) equipped with an EDAX Hikari Super ® EBSD detector.

Maps were collected at an accelerating voltage of 20 kV, probe current of 1.6 nA, working distance of ~15 mm, and with the specimen tilted at 70°. The step size was selected based on feature size: 0.2 μm for bulk grains and 50 nm for finer grains. Kikuchi patterns were acquired at a resolution of 480 × 480 pixels with 4 × 4 binning.

Indexing was performed using the EDAX OIM Analysis® software suite (version 9.0.1.277), employing the Hough transform method with the FCC and BCC structures (space groups Fm-3m and Im-3m, respectively). Post-processing included the removal of points with CI < 0.1. No artificial pattern scaling, filtering, or pattern modification was applied beyond standard background correction provided by the acquisition software.

TEM lift-outs were fabricated using an FEI Nova 200 dual-beam focused ion beam (FIB). A ~ 15 × 2 × 5 μm^3 lamella was extracted with an Omni probe micromanipulator, then thinned to ~50–100 nm by sequentially lowering Ga-ion beam voltage and current. Atom probe tomography (APT) was performed on a Cameca LEAP 5000XS in laser mode (30 ± 0.5 K, 250 kHz pulse rate, 0.005–0.01 ion/pulse detection rate, 50 pJ laser energy). Data reconstruction and analysis were conducted using Cameca AP Suite 6.1 with parameters: evaporation field 33 V/nm, field factor 3.3, and image compression factor 1.65.

Mechanical response measurements

Miniature tensile tests were conducted at a strain rate of 0.001 s^{-1} using a custom-built machine equipped with an LVDT extensometer. Dog-bone specimens with gauge dimensions of ~5 × 1 × 1 mm^3 were prepared by electric discharge machining. For each condition, three specimens were tested to ensure reproducibility.

Magnetic response measurements

Room-temperature magnetization (**M**–**H**) curves of the base CoFeNi alloy, Ti-modified $Ti_{0.24}CoFeNi_{0.78}$ CRSA, and Al, Ti-modified variants (CRSA, CRSA800, CR900) were measured using a Lakeshore 7404 vibrating sample magnetometer (VSM). For each measurement, cubic specimens of ~2 × 2 × 2 mm^3 were used. Further, each experiment was repeated thrice to check repeatability.

Resistivity measurements

Electrical resistivity was determined by the standard four-point probe method using specimens of ~2 × 1 × 5 mm^3. Resistivity values (ρ) were calculated as

$$\rho = (R \times A)/l \quad (2)$$

where R is the measured resistance, A the cross-sectional area, and l the distance between voltage contacts. For each sample, the reported resistance was averaged over four independent measurements.

Inclusion and ethics statement

This research did not involve human participants, human data, or animals. The authors affirmthat the study was conducted responsibly, with attention to integrity, transparency, and equitable collaboration.

Data availability

The data that support the findings of this study, including raw data such as a table of values for the plots, and .ang files for the EBSD scans, are available in the Source Data file. Source data are provided with this paper.

References

1. U.S. energy facts explained - consumption and production - U.S. Energy Information Administration (EIA) (2024). https://www.eia.gov/energyexplained/us-energy-facts/ (accessed December 5, 2025).
2. Aiso, K. & Akatsu, K. Performance comparison of high-speed motors for electric vehicle. *World Electr. Veh. J.* **13**, 57 (2022).
3. Byerly, K. et al. Permeability engineered soft magnetics for power dense energy conversion. In *Proc. 2021 IEEE Energy Conversion Congress and Exposition (ECCE)* 5320–5326 (IEEE, 2021) https://doi.org/10.1109/ECCE47101.2021.9594967.
4. Silveyra, J. M., Ferrara, E., Huber, D. L. & Monson, T. C. Soft magnetic materials for a sustainable and electrified world. *Science* **362**, eaao0195 (2018).
5. Fiorillo, F., Bertotti, G., Appino, C. & Pasquale, M. Soft magnetic materials. In *Wiley Encyclopedia of Electrical and Electronics Engineering* 1–42 (John Wiley & Sons, Ltd, 2016).
6. Chen, C.-W. *Magnetism and Metallurgy of Soft Magnetic Materials* (Courier Corporation, 2013).
7. Gutfleisch, O. et al. Magnetic materials and devices for the 21st century: stronger, lighter, and more energy efficient. *Adv. Mater.* **23**, 821–842 (2011).
8. Mazaleyrat, F. Soft magnetic materials and applications. In Handbook of Magnetism and Magnetic Materials (eds Coey, J. M. D. et al.) 1435–1487 (Springer International Publishing, 2021).
9. Hilzinger, H.-R. & Tenbrink, J. Soft magnetic materials: applications. In *Encyclopedia of Materials: Science and Technology* (eds Buschow, K. H. J. et al.) 8679–8684 (Elsevier, Oxford, 2001).
10. George, E. P., Gubbi, A. N., Baker, I. & Robertson, L. Mechanical properties of soft magnetic FeCo alloys. *Mater. Sci. Eng. A* **329–331**, 325–333 (2002).
11. Fingers, R. T., Carr, R. P. & Turgut, Z. Effect of aging on magnetic properties of Hiperco® 27, Hiperco® 50, and Hiperco 50 HS® alloys. *J. Appl. Phys.* **91**, 7848–7850 (2002).
12. Vahdati Yekta, P., Ghasemi, A. & Sharifi, E. M. Magnetic and mechanical properties of cold-rolled permalloy. *J. Magn. Magn. Mater.* **468**, 155–163 (2018).
13. Kim, E. S. et al. Mechanical and magnetic properties of soft magnetic Fe-Ni permalloy produced by directed energy deposition processes. *J. Mater. Sci.* **57**, 17967–17983 (2022).
14. Fingers, R. T. & Rubertus, C. S. Air force application of advanced magnetic materials. *MRS Online Proc. Libr.* **577**, 481–486 (1999).
15. Ma, M. et al. Microstructure evolution and strengthening mechanism of FeCo-1.5V0.5Nb0.4 W soft magnetic alloy rolled strip with high yield strength and low coercivity. *Acta Materialia* **268**, 119793 (2024).
16. Yeh, J.-W. et al. Nanostructured high-entropy alloys with multiple principal elements: novel alloy design concepts and outcomes. *Adv. Eng. Mater.* **6**, 299–303 (2004).
17. Cantor, B., Chang, I. T. H., Knight, P. & Vincent, A. J. B. Microstructural development in equiatomic multicomponent alloys. *Mater. Sci. Eng. A* **375–377**, 213–218 (2004).
18. Chaudhary, V., Chaudhary, R., Banerjee, R. & Ramanujan, R. V. Accelerated and conventional development of magnetic high entropy alloys. *Mater. Today* **49**, 231–252 (2021).
19. Kumari, P., Gupta, A. K., Mishra, R. K., Ahmad, M. S. & Shahi, R. R. A Comprehensive review: recent progress on magnetic high entropy alloys and oxides. *J. Magn. Magn. Mater.* **554**, 169142 (2022).
20. Lamichhane, T. N. et al. Additive manufacturing of soft magnets for electrical machines—a review. *Mater. Today Phys.* **15**, 100255 (2020).
21. Dasari, S. et al. Hierarchical eutectoid nano-lamellar decomposition in an $Al_{0.3}$CoFeNi complex concentrated alloy. *Sci. Rep.* **10**, 4836 (2020).
22. Dasari, S. et al. Highly tunable magnetic and mechanical properties in an Al0.3CoFeNi complex concentrated alloy. *Materialia* **12**, 100755 (2020).
23. Wang, W.-R., Wang, W.-L. & Yeh, J.-W. Phases, microstructure and mechanical properties of AlxCoCrFeNi high-entropy alloys at elevated temperatures. *J. Alloy. Compd.* **589**, 143–152 (2014).
24. Kovács, A. et al. Role of heterophase interfaces on local coercivity mechanisms in the magnetic Al0.3CoFeNi complex concentrated alloy. *Acta Materialia* **246**, 118672 (2023).
25. Manzoni, A., Daoud, H., Völkl, R., Glatzel, U. & Wanderka, N. Phase separation in equiatomic AlCoCrFeNi high-entropy alloy. *Ultramicroscopy* **132**, 212–215 (2013).
26. Richard, M. B. Iron nickel alloys. In *Ferromagnetism* 102–189 (IEEE, 1978).
27. Dasari, S., Sharma, A., Gorsse, S., Chesetti, A. & Banerjee, R. Non-classical nucleation of ordered L12 precipitates in the FCC based Al0.25CoFeNi high entropy alloy. *J. Appl. Phys.* **134**, 015102 (2023).
28. Tan, L. P., Chaudhary, V., Tsakadze, Z. & Ramanujan, R. V. Rapid multiple property determination from bulk materials libraries prepared from chemically synthesized powders. *Sci. Rep.* **12**, 9504 (2022).
29. Wang, L. et al. Microstructure and mechanical property of novel L12 nanoparticles-strengthened CoFeNi-based medium entropy alloys. *Mater. Sci. Eng.: A* **840**, 142917 (2022).
30. Liu, X. W. et al. The role of carbon in grain refinement of cast CrFeCoNi high-entropy alloys. *Metall. Mater. Trans. A* **49**, 2151–2160 (2018).
31. Wang, Z., Baker, I., Guo, W. & Poplawsky, J. D. The effect of carbon on the microstructures, mechanical properties, and deformation mechanisms of thermo-mechanically treated Fe40.4Ni11.3Mn34.8Al7.5Cr6 high entropy alloys. *Acta Materialia* **126**, 346–360 (2017).
32. Slone, C. E., Miao, J. & Mills, M. J. Ultra-high strength and ductility from rolling and annealing of a Ni-Cr-Co superalloy. *Scr. Materialia* **155**, 94–98 (2018).
33. Chen, Y. et al. Tailoring microstructures and tensile properties of a precipitation-strengthened (FeCoNi)94Ti6 medium-entropy alloy. *J. Alloy. Compd.* **828**, 154457 (2020).
34. Gwalani, B. et al. Optimizing the coupled effects of Hall-Petch and precipitation strengthening in a $Al_{0.3}$CoCrFeNi high entropy alloy. *Mater. Des.* **121**, 254–260 (2017).
35. Du, X. H. et al. Dual heterogeneous structures lead to ultrahigh strength and uniform ductility in a Co-Cr-Ni medium-entropy alloy. *Nat. Commun.* **11**, 2390 (2020).
36. Gwalani, B. et al. High density of strong yet deformable intermetallic nanorods leads to an excellent room temperature strength-ductility combination in a high entropy alloy. *Acta Materialia* **219**, 117234 (2021).
37. Reed, R. C., Matan, N., Cox, D. C., Rist, M. A. & Rae, C. M. F. Creep of CMSX-4 superalloy single crystals: effects of rafting at high temperature. *Acta Materialia* **47**, 3367–3381 (1999).
38. Yu, J. et al. A two-stage predicting model for γ′ solvus temperature of $L1_2$-strengthened Co-base superalloys based on machine learning. *Intermetallics* **110**, 106466 (2019).
39. Suzuki, A., Inui, H. & Pollock, T. M. L12-strengthened cobalt-base superalloys. *Annu. Rev. Mater. Res.* **45**, 345–368 (2015).
40. Zhang, B. B., Yan, F. K., Zhao, M. J., Tao, N. R. & Lu, K. Combined strengthening from nanotwins and nanoprecipitates in an iron-based superalloy. *Acta Materialia* **151**, 310–320 (2018).
41. Zuo, T., Ren, S., Liaw, P. K. & Zhang, Y. Processing effects on the magnetic and mechanical properties of $FeCoNiAl_{0.2}Si_{0.2}$ high entropy alloy. *Int. J. Min. Met. Mater.* **20**, 549–555 (2013).
42. Masteller, M. S., Bowman, J. W. & Li, L. High temperature aging behavior of high strength 49%Co-1.9%V-0.3%Nb-Fe soft magnetic alloy. *IEEE Trans. Magn.* **32**, 4839–4841 (1996).

43. Han, L. et al. Ultrastrong and ductile soft magnetic high-entropy alloys via coherent ordered nanoprecipitates. *Adv. Mater.* **33**, 2102139 (2021).
44. Xu, X. et al. Improvement in mechanical as well as magnetic properties of a (FeCoNi)90Ti10-*x*Al*x* complex concentrated alloy series by tuning the chemical order. *Scr. Materialia* **254**, 116333 (2025).
45. Wang, W.-R. et al. Effects of Al addition on the microstructure and mechanical property of AlxCoCrFeNi high-entropy alloys. *Intermetallics* **26**, 44–51 (2012).
46. Dasari, S. et al. Recovery of cold-worked $Al_{0.3}$CoCrFeNi complex concentrated alloy through twinning assisted B2 precipitation. *Acta Materialia* **202**, 448–462 (2021).
47. He, J. Y. et al. A precipitation-hardened high-entropy alloy with outstanding tensile properties. *Acta Materialia* **102**, 187–196 (2016).
48. Dasari, S. et al. Exceptional enhancement of mechanical properties in high-entropy alloys via thermodynamically guided local chemical ordering. *Proc. Natl. Acad. Sci. USA* **120**, e2211787120 (2023).
49. Sharma, S. et al. Laser based additive manufacturing of tungsten: multi-scale thermo-kinetic and thermo-mechanical computational model and experiments. *Acta Materialia* **259**, 119244 (2023).
50. Chaudhary, V. et al. Additive manufacturing of functionally graded Co–Fe and Ni–Fe magnetic materials. *J. Alloy. Compd.* **823**, 153817 (2020).
51. Han, L. et al. Strong and ductile high temperature soft magnets through Widmanstätten precipitates. *Nat. Commun.* **14**, 8176 (2023).
52. Han, L. et al. A mechanically strong and ductile soft magnet with extremely low coercivity. *Nature* **608**, 310–316 (2022).
53. Li, P., Wang, A. & Liu, C. T. Composition dependence of structure, physical and mechanical properties of FeCoNi(MnAl)x high entropy alloys. *Intermetallics* **87**, 21–26 (2017).
54. Han, L. et al. Two-gigapascal-strong ductile soft magnets. *Nat. Commun.* **15**, 10119 (2024).
55. Reed, R. C. *The Superalloys: Fundamentals and Applications* (Cambridge Univ. Press, Cambridge, 2006).
56. Sarkar, S. K. & Biswas, A. APT based reliable quantification of Cr-rich phase separation and its relationship with mechanical properties in thermally aged Fe-20 at.% Cr alloy. *J. Nucl. Mater.* **572**, 154090 (2022).
57. Li, P., Wang, A. & Liu, C. T. A ductile high entropy alloy with attractive magnetic properties. *J. Alloy. Compd.* **694**, 55–60 (2017).
58. Chen, C. et al. A novel ultrafine-grained high entropy alloy with excellent combination of mechanical and soft magnetic properties. *J. Magn. Magn. Mater.* **502**, 166513 (2020).

Acknowledgements

The work was supported by the U.S. Air Force Office of Scientific Research under Grant Nos. FA9550–17–1–0395 (RB), FA9550–21–1–0304 (RB), and by the Center for Agile and Adaptive and Additive Manufacturing (CAAAM), at the University of North Texas, funded through State of Texas Appropriation: 190405-105-805008-220 (NBD). The authors would like to acknowledge the Materials Research Facility (MRF) for access to advanced characterization techniques. The authors also acknowledge the support of the AME Programmatic Fund by the Agency for Science, Technology and Research, Singapore, under Grant Nos. A1898b0043 (RVR) and A18B1b0061 (RVR), and Production Area of Advance (AoA) at Chalmers University of Technology. Additionally, part of this research is supported by the National Research Foundation, Singapore, under its 29th Competitive Research Program (CRP) Call (Award ID NRF-CRP29-2022-0002) (RVR).

Author contributions

S.K.S., N.K.: Conceptualization, Methodology, Validation, Formal analysis, Investigation, Data curation, Writing – Original Draft, Writing – Review & Editing. L.P.T., T.I., A.C., S.D.: Validation, Formal analysis, Investigation, Data curation. K.P.D., V.C., N.D., R.V.R., R.B.: Conceptualization, Supervision, Project administration, Funding acquisition, Resources, Writing – Review & Editing.

Competing interests

The authors declare no competing interests.

Additional information

Supplementary information The online version contains supplementary material available at https://doi.org/10.1038/s41467-026-68891-6.

Correspondence and requests for materials should be addressed to V. Chaudhary, R. V. Ramanujan or Rajarshi Banerjee.

Peer review information *Nature Communications* thanks Priyanka Kumari, Jiawei Li, and the other anonymous reviewer(s) for their contribution to the peer review of this work. A peer review file is available.